ADVANCES IN ATMOSPHERIC SCIENCES, VOL. 35, MARCH 2018, 296–316

• **Original Paper** •

Statistics-based Optimization of the Polarimetric Radar Hydrometeor Classification Algorithm and Its Application for a Squall Line in South China

Chong WU[1,2], Liping LIU[*2], Ming WEI[1], Baozhu XI[1,2], and Minghui YU [2]

[1]*Collaborative Innovation Center on Forecast and Evaluation of Meteorological Disasters, Nanjing University of Information Science and Technology, Nanjing* 210044*, China*

[2]*State Key Lab of Severe Weather, Chinese Academy of Meteorological Science, Beijing* 100081*, China*

(Received 16 September 2016; revised 4 July 2017; accepted 11 July 2017)

ABSTRACT

A modified hydrometeor classification algorithm (HCA) is developed in this study for Chinese polarimetric radars. This algorithm is based on the U.S. operational HCA. Meanwhile, the methodology of statistics-based optimization is proposed including calibration checking, datasets selection, membership functions modification, computation thresholds modification, and effect verification. Zhuhai radar, the first operational polarimetric radar in South China, applies these procedures. The systematic bias of calibration is corrected, the reliability of radar measurements deteriorates when the signal-to-noise ratio is low, and correlation coefficient within the melting layer is usually lower than that of the U.S. WSR-88D radar. Through modification based on statistical analysis of polarimetric variables, the localized HCA especially for Zhuhai is obtained, and it performs well over a one-month test through comparison with sounding and surface observations. The algorithm is then utilized for analysis of a squall line process on 11 May 2014 and is found to provide reasonable details with respect to horizontal and vertical structures, and the HCA results—especially in the mixed rain–hail region—can reflect the life cycle of the squall line. In addition, the kinematic and microphysical processes of cloud evolution and the differences between radar-detected hail and surface observations are also analyzed. The results of this study provide evidence for the improvement of this HCA developed specifically for China.

Key words: dual polarization radar, hydrometeor classification, fuzzy logic scheme

Citation: Wu, C., L. P. Liu, M. Wei, B. Z. Xi, and M. H, Yu, 2018: Statistics-based optimization of the polarimetric radar Hydrometeor Classification Algorithm and its application for a squall line in South China. *Adv. Atmos. Sci.*, **35**(3), 296–316, https://doi.org/10.1007/s00376-017-6241-0.

1. Introduction

In the measurements of conventional radar, precipitation particles absorb and scatter the horizontally polarized electromagnetic pulse. The echo power received from the backscattering cross section and the Doppler shift are used to calculate the reflectivity factor (Z) and radial velocity (V). However, it is hard to identify the particles in different phases since the magnitude of Z from raindrops or snow is almost the same. A dual-polarization weather radar can transmit and receive both horizontally and vertically polarized radiation simultaneously, which makes it capable of obtaining not only the Z and V, but also the differential reflectivity ($Z_{\rm DR}$), differential phase ($\Phi_{\rm DP}$), specific differential propagation phase ($K_{\rm DP}$), linear depolarization ratio ($L_{\rm DR}$) and correlation coefficient ($\rho_{\rm hv}$). Particles can be identified based on characteristics of polarimetric variables, and this hydrometeor classification algorithm (HCA) principle is also the main advantage of dual-polarization radar. Schuur et al. (2003) clearly indicated that polarimetric radar can detect various phases of precipitation particles, especially hail in strong convective systems and signatures of tornado debris, in their JPOLE (Joint Polarization Experiment) report. This is particularly important for nowcasting and microphysics research.

In early studies of hydrometeor classification, Straka et al. (1993) and Straka (1996) found that the method used to discriminate overlapping polarimetric variables from various precipitation types directly affects the classification accuracy. Therefore, the fuzzy logic approach was chosen due to its simple and straightforward functions and the ease with which it can be improved. Five polarimetric variables (Z, $Z_{\rm DR}$, $\rho_{\rm hv}$, $K_{\rm DP}$, $L_{\rm DR}$) were used by Zrnić and Ryzhkov (1999) to identify hydrometeor classes of drizzle (DZ), moderate light and moderate rain (RA), heavy rain (HR), hail, a mixture of rain and hail (RH), graupel (GR), wet snow (WS), dry snow

* Corresponding author: Liping LIU
E-mail: lpliu@camscma.cn

(DS), and ice crystals (CR). Also, in their study, they applied semi-empirical membership functions, and subjective weighting factors. However, a fixed melting layer was used in this method, and the supercooled water droplets above this level were not considered. Vivekanandan et al. (1999) proposed a more complicated method based on 2D membership functions. For this Particle Identification Algorithm (PID), a smooth transitional region was enclosed by Z and another polarimetric variable to increase the identification accuracy. Lim et al. (2005) used β-type membership functions and introduced the height membership function as the sixth threshold. Also, their freezing altitude was no longer a fixed level; rather, it was identified based on environmental conditions. To obtain more accurate results, Zrnić and Ryzhkov (1999) investigated the sensitivity of polarimetric variables in the fuzzy logic approach, and found that Z and Z_{DR} are two robust variables for the classification of hydrometeors among the five polarimetric variables of Z, Z_{DR}, ρ_{hv}, K_{DP} and L_{DR}. They also pointed out that the addition of temperature profiles into the classification can effectively eliminate many of the errors in the result. Based on the fuzzy logic approach, Liu and Chandrasekar (2000) calculated the scope of the membership functions through a neural network, which could reduce the influences of observation errors caused by radar hardware. However, the "true value" of the training set for the neural network is hard to obtain, which limits the application of this method. Notably, in all the above classification methods, the confidence factor, which reflects the quality of polarimetric observations, is not considered.

With improvements in HCAs, the quality of polarimetric observations has become the major factor that affect the reliability of classification. Ryzhkov et al. (2005) found that if the calibration errors of Z and Z_{DR} are larger than 1 dB and 0.2 dB, respectively, all algorithm calculations containing these two variables will be affected. Giangrande and Ryzhkov (2005) suggested that partial beam blockage has significant impacts on Z and Z_{DR} for all azimuths, and the largest error of Z_{DR} can be up to 0.8 dB at the elevation angle of 0.5°. To reduce the impact of errors caused by low quality observations, Park et al. (2009) at the National Severe Storm Laboratory proposed a new fuzzy logic–based HCA, in which the confidence level was calculated to evaluate the quality of the radar observations for each polarimetric variable, and could be used to adjust the weighting factors during the fuzzy logic approach. The operational algorithm uses the HCA for the U.S. Weather Surveillance Radar 88 Doppler (WSR-88D) dual-polarization radars, the results of which have been widely verified (Elmore, 2011; Zhang et al., 2011; Schuur et al., 2012; Zhang et al., 2012).

In China, preliminary studies on dual-polarization radar started from the 1990s, and a polarimetric radar prototype was applied to hail detection and precipitation estimation at that time (Liu et al., 1992, 1996). Since 2000, several C-band and X-band dual-polarization radars have been deployed by the Chinese Academy of Meteorological Science (CAMS), Wuhan Institute of Heavy Rain, Beijing Meteorology Bureau, Qingdao Meteorology Bureau, and Shanghai Meteorology Bureau for scientific research purposes and the support of major public events such as the Beijing Olympic Games and the Shanghai World Expo (Xiao et al., 2012; Hu et al., 2014, 2015; Liu et al., 2016; Wei et al., 2016). At the time, the corresponding algorithm was developed based on analysis of outfield experiments (Su et al., 2011; Liu et al., 2012). With improvements in radar technology and meteorological services in China, the new generation of weather radars (CINRAD), deployed since 2000, will be gradually updated to dual-polarization radars. From 2014 to 2017, six operational polarimetric radars were deployed in South China to monitor heavy rainfall, which can cause serious damage and losses to lives and properties, on an annual basis. The China Meteorological Administration (CMA) carried out the Southern China Monsoon Rainfall Experiment in 2013, which was aimed at better understanding the initiation and dissipation of mesoscale convective systems, improving high-resolution weather forecasts and severe weather event warnings, and providing better safeguard capabilities for economic zones over South China (Luo et al., 2016). From previous studies in this era, single-polarization radar observations were utilized to reveal the structures and spatiotemporal characteristics of precipitation (Pan et al., 2010; Chen et al., 2014; Wang et al., 2014; Chen et al., 2015, Chen et al., 2016). As more polarimetric radars are applied for operational weather services in the future, two questions should be addressed: (1) How can we develop a HCA that is appropriate specifically for Chinese radar hardware and precipitation characteristics? (2) What are the effects of such a localized HCA when it is applied for research and nowcasting?

In this study, a modified HCA for Chinese operational radars is proposed based on the HCA of the U.S. Through a series of procedures, parameters and thresholds in the HCA are optimized to be suitable for the Zhuhai polarimetric radar in South China, and the changes to this algorithm are verified against soundings and surface observations. Subsequently, the algorithm is applied to investigate the evolution and microphysical processes of a squall line that occurred on 11 May 2014.

2. Basic principles of the HCA

In the original HCA (Park et al., 2009), radar echoes are classified into 10 classes: (1) ground clutter or anomalous propagation (GC/AP); (2) biological scatterers (BS); (3) DS); (4) WS; (5) CR; (6) GR; (7) "big drops" (BD); (8) RA; (9) HR; and (10) RH. The BD corresponding to the type of precipitation contain large amounts of drops with diameter greater than 3 mm, and small drops are rare in the drop size distribution (DSD). According to Wakimoto and Bringi (1988) and Kumjian and Ryzhkov (2008), BD are often associated with supercooled water in updrafts. The six radar variables used for hydrometeor classification are: (1) Z; (2) Z_{DR}; (3) ρ_{hv}; (4) K_{DP}; (5) standard deviation of Z [SD(Z)]; and (6) standard deviation of Φ_{DP} [SD(Φ_{DP})]. The first four variables directly reflect the hydrometeor phase, while the last two are

mainly applied in distinguishing non-meteorological echoes. Figure 1 presents the flowchart of the HCA.

Compared with the PID algorithm proposed by Vivekanandan et al. (1999), four extra procedures (confidence vector calculation, meting layer detection, precipitation type identification, and empirical thresholds checking) are added to the HCA algorithm. The confidence vector can reduce the impact on low-reliability polarimetric variables, which are often caused by noise and errors. The other three procedures can be used to adjust the classification results based on the level of the melting layer, the precipitation features associated with convective or stratiform clouds, and characteristics of polarimetric variables corresponding to typical hydrometeors. As a result, these procedures greatly improved the reliability of the HCA algorithm. Based on the fuzzy logic principle, an aggregation value of A_i for the ith class of radar echoes is defined as

$$A_i = \frac{\sum_{j=1}^{6} W_{i,j} Q_j P_i(V_j)}{\sum_{j=1}^{6} W_{i,j} Q_j}, \quad (1)$$

where V_j is the jth variable, and $P_i(V_j)$ is a membership function that characterizes the distribution of the jth variable for the ith class. Here, the membership function $P_i(V_j)$ is assumed to have trapezoidal shape. Value of the functions is determined by the relative location between the input variable and the trapezoidal-shaped membership functions, where different parameters correspond to distributions of the polarimetric variables of different hydrometeors. $W_{i,j}$ is a weight between 0 and 1 assigned to the jth variable. It describes the discriminating efficiency of each variable with respect to a particular class.

In the HCA, the confidence vector (Q_j) is used to account for the impact of measurement errors on the jth variable. According to Ryzhkov (2007), Φ_{DP} represents the impact of errors induced by radar attenuation; the signal-to-noise ratio (SNR) reflects the impact of receiver noise; ρ_{hv} indicates the effects of statistical errors of polarimetric variables; and the gradients of variables indicate the impact of nonuniform beam filling. The impact of errors will increase with increases in Φ_{DP} and larger gradients of the variables or decreases in SNR and ρ_{hv}. As a result, the radar data quality will become lower and the corresponding confidence level will decrease too, which is equivalent to assigning a lower weighting factor in the fuzzy logic calculation. A Gaussian function with the center located at the y-axis and Φ_{DP}, SNR, ρ_{hv} and gradients as variables on the x-axis, was used in the computation of the confidence vector. Four basic confidence functions, i.e. $Q(\Phi_{DP})$, Q(SNR), $Q(\rho_{hv})$, and Q(gradients) are constructed as products of Gaussian functions controlled by thresholds. Since the extent to which these variables can be affected by errors is different (e.g., attenuation has little impact on K_{DP}, and Z is not affected by statistical errors of polarimetric variables), the confidence vector is obtained as a product with different computing thresholds. This method of dynamic weight based on observations can effectively ensure the reliability of the hydrometeor classification for biased and noisy measurements.

3. HCA optimization methodology

Based on the studies of Heinselman and Ryzhkov (2006), measurements of WSR-88D polarimetric radar in Oklahoma were used to verify and optimize the results of the HCA. Considering that the DSD changes at different regions (Jameson et al., 2015; Jameson, 2016) and radar hardware differences can affect the polarimetric measurements, the membership function P and confidence vector Q in the HCA are not fixed. It is necessary to analyze the quality of polarimetric variables from local observations and optimize the membership functions and confidence vector thresholds based on statistics of

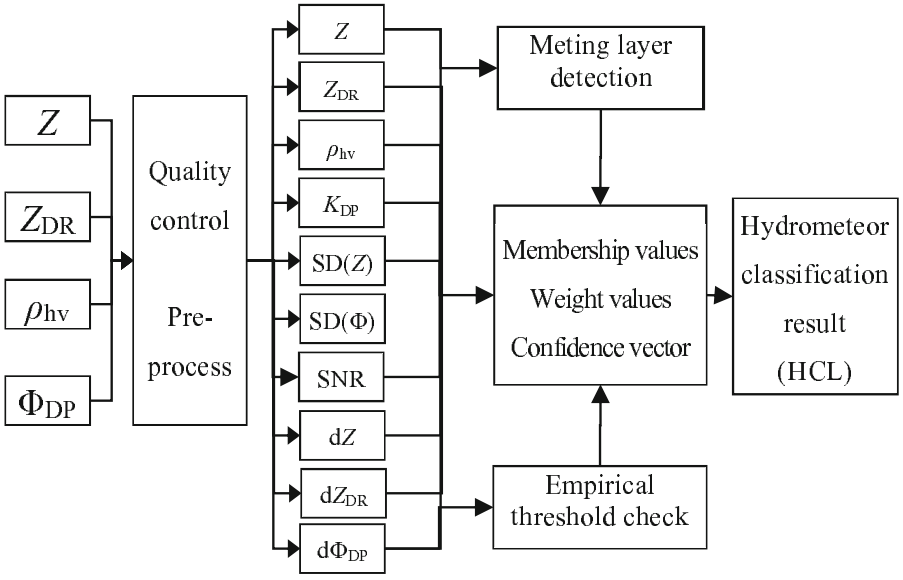

Fig. 1. Flowchart of the HCA.

common hydrometeors classes. In this section, a localized HCA that is specialized for the Zhuhai radar hardware and the precipitation characteristics over South China is proposed through statistical methods, and its results validated. As more polarimetric radars are deployed in South China (e.g., at Foshan and Lianzhou), the optimization and verification procedures presented below could also be applied to them for their specific HCAs.

3.1. *Zhuhai radar and its calibration*

The Zhuhai radar used in this study is an output of a collaborative project between the CMA and Guangdong Provincial Government for the establishment of meteorology modernization. It is also a key project in the Cooperation Framework Agreement of Guangdong and Macao. The Zhuhai radar was deployed at Jiaoding Mountain, Sanzhao town, Zhuhai (22.03°N, 113.37°E) in late September 2012, and was put into operation in December 2013. It plays a critical role in monitoring severe weather events over Zhuhai, Macao and other regions of the Pearl River Delta. The S-band dual-polarization radar, produced by Beijing Metstar Co Ltd, is the first operational dual-polarization radar in China, and its capability and signal processing system are at an advanced level compared to other Chinese radars. Table 1 lists the major parameters of the Zhuhai radar.

The calibration accuracy is a critical factor for the operational application of polarimetric radars. If the systematic bias of Z, Z_{DR} or ρ_{hv} is large enough, the reliability of classification results will be correspondingly reduced. After the construction of the Zhuhai radar, a series of tests were conducted by the Meteorological Observation Center of the CMA and the results indicated that the radar hardware is almost accurate. Meanwhile, statistical data methods based on routine observations such as vertical scanning, echoes from light rain and dry snow, and comparison with nearby radars, can also be utilized for the inspection of calibration effects. In this paper, light rain and dry snow echoes from stratiform precipitation cases during May 2014 are collected for statistical sampling because the VCP21D volume scan mode does not provide vertical pointing observations. The frequency distribution plot of Z between Zhuhai and Guangzhou radar is shown in Fig. 2a (Guangzhou radar is a single-polarization radar located 90 km away from the northwest of Zhuhai). Histograms of Z_{DR} and ρ_{hv} calculated from light rain where Z ranges between 15 and 20 dBZ below the altitude of 3 km, and from dry snow where Z ranges between 15 and 25 dBZ above the altitude of 5 km, are shown in Figs. 2b–e, respectively. The results reveal that there is little difference in Z between Guangzhou and Zhuhai radars. The mean Z_{DR} from light rain and dry snow echoes is 0.41 dB and 0.35 dB. Their ρ_{hv} is close to 1 within reasonable values. The result serves as evidence that the systematic bias of Z_{DR} is ~0.38 dB; therefore, calibration correction is conducted on the Zhuhai radar before data processing.

Table 1. Parameters of the Zhuhai dual polarization radar.

Variable	Parameter
Antenna diameter (m)	8.54
Antenna gain (dB)	45.31
Bean width (°)	< 0.98
First side lobe (dB)	< 30
Isolation (dB)	⩾ 40
Wavelength (cm)	10.3
Pulse width (μs)	1.57
Peak power (kW)	800
Pulse repetition frequency (Hz)	250–1304
Operating mode	SHV
Minimum detectable power (dBm)	−117.8
Noise (dB)	2
Dynamic range (dB)	> 95
Volume scan mode	VCP21D

3.2. *Data pre-processing and statistical region selection*

Z, Z_{DR}, ρ_{hv} and Φ_{DP} in the raw radar data cannot be directly used in the classification algorithm. First, quality control must be conducted to ensure the accuracy of the input data for the algorithm. This includes noise suppression with a 1-km running-average filter and identification of $\Phi_{DP}(0)$ and estimation of K_{DP} by the filtering of Φ_{DP}, for example. Since the attenuation by rain has little impact on S-band radar, it is not necessary to perform attenuation correction for Z and Z_{DR}. After pre-processing, the quality-controlled radar data are obtained, where Z, Z_{DR}, ρ_{hv}, K_{DP}, SD(Z) and SD(Φ_{DP}) are used in the fuzzy logic scheme, and Φ_{DP}, SNR, ρ_{hv} and gradients of variables (dZ, dZ_{DR}, dΦ_{DP}) are used for confidence vector computation.

Figure 3 displays horizontal profiles of Z, Z_{DR}, ρ_{hv} and SNR changes with radial distance before and after the filtering from Zhuhai radar measurements at 4.3° elevation and 325° azimuth at 2140 LST (local standard time) 9 May 2014. The results clearly show that fluctuations exist in the raw radar data due to disturbances in the atmosphere and internal noise of the radar system. In particular, the dynamic ranges of Z_{DR} and ρ_{hv} are small, meaning fluctuations in the raw data will affect the stability of the classification algorithm and lead to incorrect results. After passing through the averaging filter, fluctuations in the raw radar data can be considerably suppressed, and the variables can better correspond to meteorological targets. However, significant fluctuations in Z_{DR} and ρ_{hv} still exist beyond 90 km after the filtering. Considering the SNR here is lower than 20 dB, this phenomenon is attributed to measurement errors caused by the inconsistency between the two channels when the signal is weak.

This is the time when large-scale stratiform precipitation occurred. The radar beam reaches an altitude of 10 km after propagating about 120 km at an elevation of 4.3°. Changes in polarimetric variables with distance can reflect hydrometeor information at various heights. According to the microphysical process involved in stratiform precipitation, ice crystals and snowflakes melt on their surface when they fall near the 0°C height. These ice crystals and snowflakes collide and

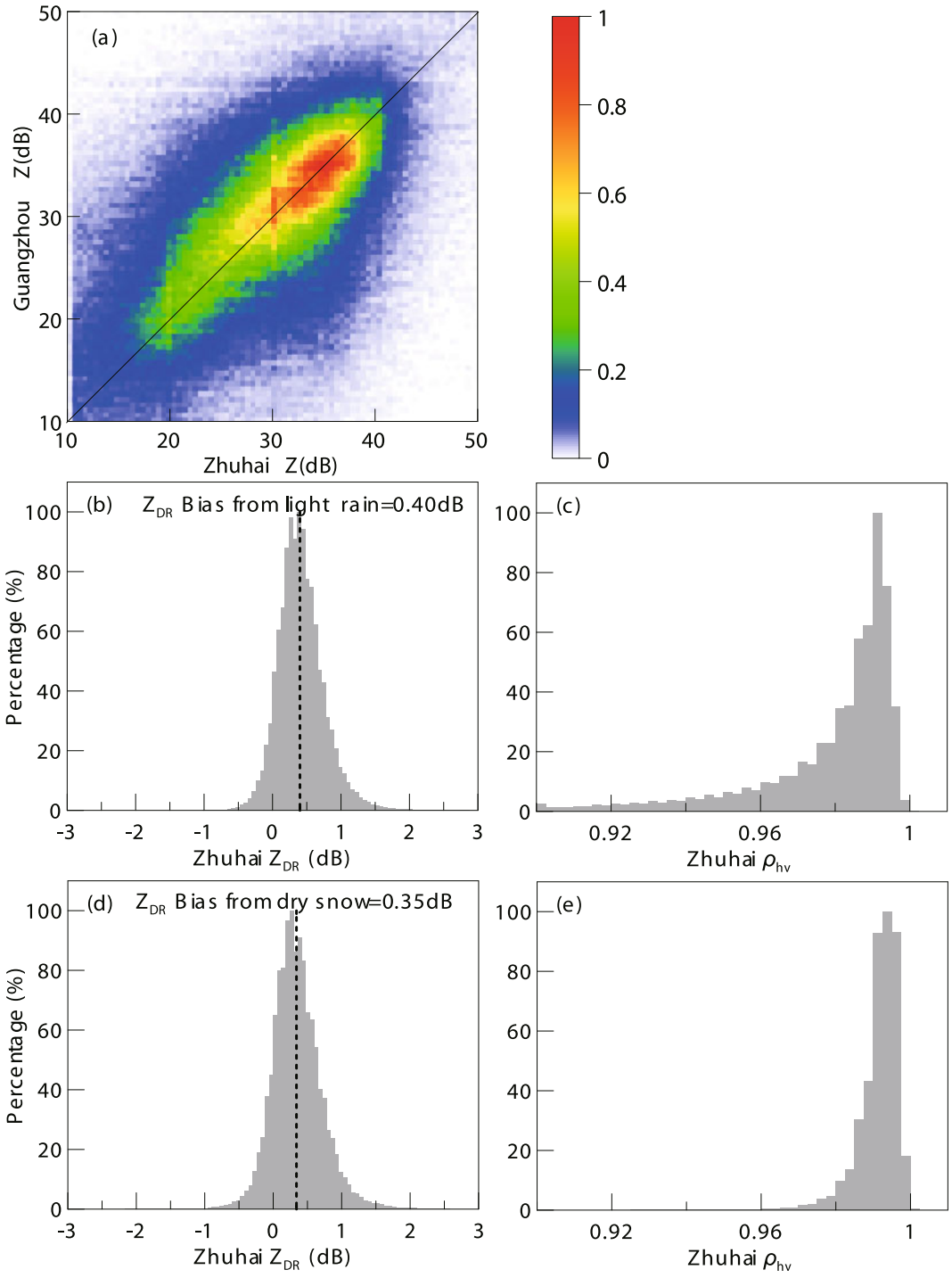

Fig. 2. Calibration effects of Zhuhai radar: (a) frequency distribution plot of Z between Zhuhai and Guangzhou radar; (b) histogram of Z_{DR} from light rain; (c) histogram of ρ_{hv} from light rain; (d) histogram of Z_{DR} from dry snow; (e) histogram of ρ_{hv} from dry snow.

stick together, forming melted aggregates. Changes in the dielectric constant and increases in the volume lead to increases in Z and Z_{DR} at various degrees, whereas the transformation in the scattering property will cause the decreases in ρ_{hv}. As a result, a distinct bright band occurs around the melting layer, which is denoted in Fig. 3 by gray dashed lines. Based on the above microphysical processes and melting-layer features, the volume scanning of Zhuhai radar during stratiform precipitation cases can be artificially divided into three subregions: snow and ice crystal mixing region; melting region; and pure raindrops region according to the sounding height. These three sub-regions correspond to the classes of DS and CR, WS, and RA described in the HCA. Subsequently, the polarimetric characteristics of hydrometeors within each sub-

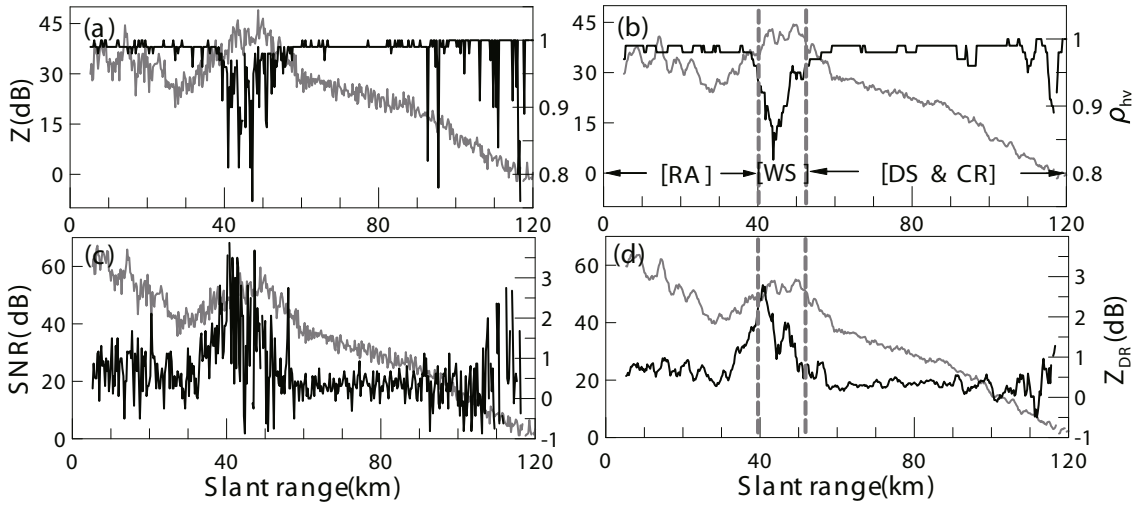

Fig. 3. Profiles of (a, b) Z and ρ_{hv} and (c, d) Z_{DR} and SNR changes with radial distance before and after the filtering from Zhuhai radar measurements at an elevation of 4.3° and azimuth of 325° at 2140 LST 9 May 2014: (a, c) raw data; (b, d) filtered data. Black lines denote ρ_{hv} and Z_{DR}; gray lines denote Z and SNR; gray dashed lines indicate the melting layer.

region can be analyzed.

3.3. *Adjustment of confidence vector based on echo statistics*

Weight adjustment of the confidence vector Q completely depends on routine observations. If the distribution of polarimetric variables obtained from Zhuhai radar is different from that of the U.S. WSR-88D radar, then the Q computed using the original parameters in the HCA cannot correctly reflect the real data quality. Since the difference in radar hardware is largely reflected in receiver noise and statistical errors, the two variables of ρ_{hv} and SNR, which are utilized for confidence vector computation, would accordingly produce the quality-control effects on the functions Q(SNR) and $Q(\rho_{hv})$. For this reason, the relationships of SNR with Z_{DR} and ρ_{hv} are investigated through the DS echoes less than 25 dBZ from Zhuhai radar measurements above 5 km in altitude. The results are shown in Figs. 4a and b.

The frequency distribution plot indicates that the majority of Z_{DR} points locate in the range of 0–0.5 dB, while ρ_{hv} is larger than 0.98. Both of them are in reasonable scopes considering that these points are concentrated over higher SNR regions. However, the scatter increases with the decreasing SNR, and large scatter occurs when SNR is less than 20 dB, which indicates that for weak-signal conditions, the receiver noise can affect the reliability of polarimetric variables. The U.S. WSR-88D radar provides relatively high-quality data, and the default Q(SNR) function has a value larger than 0.85 for SNR > 10 dB, and larger than 0.5 for SNR > 5 dB, as shown in Fig. 4c by the gray solid line. Apparently, for the relatively low-quality data from Zhuhai radar where the SNR is within 10–20 dB, its SNR confidence is mistakenly overestimated. To make Q(SNR) correctly match with the Zhuhai radar hardware, the minimum confidence value of 0.85 for the default membership functions of meteorological objects is taken as the lower limit (black dashed lines in Fig. 4c), which is also considered as the optimization criteria. After the modification, the confidence value for Q(SNR) is lowered to 0.85 at 20 dB, and to 0.5 at 10 dB (black solid line). Compared with the pre-modified Q, the optimized confidence vector does not affect the weight for normal echoes, while the confidence level for weak signals is greatly reduced.

Similarly, Fig. 4d presents the default $Q(\rho_{hv})$ from the U.S. Considering that the lower limit of default ρ_{hv} membership functions (i.e., WS or RH) is around 0.9, the minimum confidence level of meteorological echoes is also about 0.85. When $\rho_{hv} < 0.9$, statistical errors of polarimetric variables increase and $Q(\rho_{hv})$ decreases from 0.85 to 0.5. However, different from the $Q(Z_{DR})$, the ρ_{hv} threshold of 0.8 is regarded as the demarcation value between meteorological and non-meteorological echoes. When ρ_{hv} is less than 0.8, $Q(\rho_{hv})$ is compulsorily increased to 1 to avoid the weight for non-meteorological echoes being abnormally low. It is found that the SNR from Zhuhai measurements for WS is basically larger than 40 dB, while the ρ_{hv} is significantly lower with 90% of the spots ranged from 0.84 to 0.98, and the lowest ρ_{hv} is close to 0.7. Thereby, the confidence threshold for ρ_{hv} needs to be lowered. The ρ_{hv} value is reduced from 0.9 to 0.84 for those spots with $Q(\rho_{hv})$ greater than 0.85. Meanwhile, the demarcation value between meteorological and non-meteorological echoes is reduced from 0.8 to 0.75. These above changes could better solve the problem of improper weighting during confidence vector computation for the Zhuhai radar.

3.4. *Adjustment of membership functions based on echo statistics*

To evaluate the default membership functions of the HCA, polarimetric variables in the snow and ice mixing region, melting region, and pure raindrops region are extracted

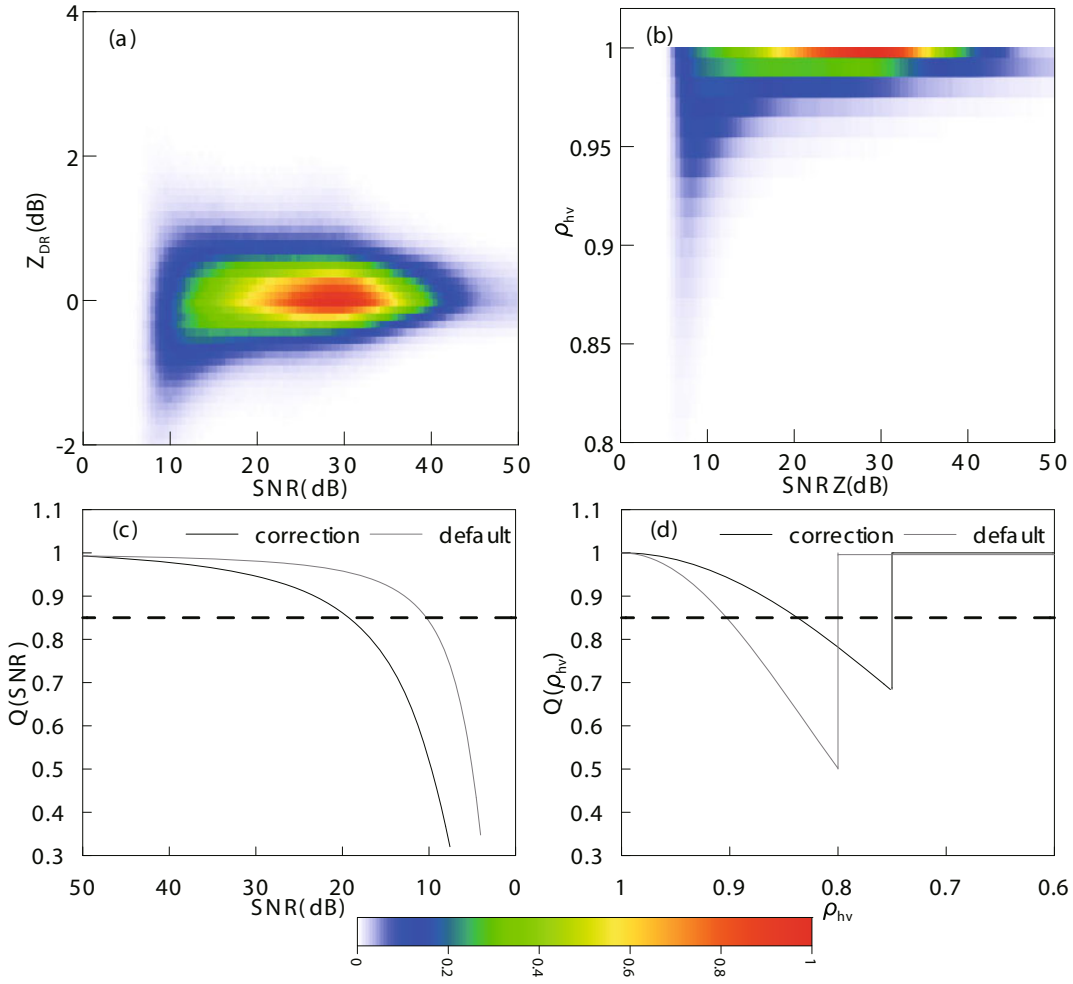

Fig. 4. Analysis of data quality and its confidence vector from Zhuhai radar: (a) frequency distribution plot of SNR-Z_{DR} from dry snow; (b) frequency distribution plot of SNR-ρ_{hv} from dry snow; (c) functions of confidence vector at default and modified SNR thresholds; (d) functions of confidence vector at default and modified ρ_{hv} thresholds.

from observations based on the distinctly different microphysical processes described in section 3.2. According to the melting characteristics of Z, Z_{DR} and ρ_{hv}, the radial distance of each hydrometeor could be manually determined, and their statistical distributions are analyzed and the results are shown in the frequency distribution plots of Z–Z_{DR} and Z–ρ_{hv} (Figs. 5a–f). Large-scale stratiform precipitation observations of Zhuhai radar during 1002–1105 and 2126–2233 LST 9 May 2014 are used for this analysis. Ground clutter, other noisy echoes, and data with SNR < 20 dB are all filtered out. Furthermore, the echoes of BS, which are possibly caused by Bragg Scattering according to recent research (Lindsey et al., 2017), are also analyzed to improve the non-meteorological echo suppression. The frequency distribution plots of SD(Z)–SD(Φ_{DP}) and SD(Z)–ρ_{hv} are shown in Figs. 5g and h, respectively.

The default range corresponding to the upper edge of the trapezoidal shape is linked by red lines in Fig. 5. Within the area enclosed by the red lines, the value of the membership function for a specific class is 1. Similarly, the default range corresponding to the bottom edge of the trapezoidal shape is linked by dashed red lines. In the transitional zone from solid to dashed red lines, the value of the membership functions gradually reduces from 1 to 0, and the value beyond the enclosed area of the dashed red lines is 0. Thereby, the precipitation particles of a specific class are largely concentrated in the area enclosed by the solid lines, and cannot appear beyond the area enclosed by the dashed lines. According to this principle, the membership functions can be optimized based on the relative location between dots and the enclosed areas.

The difference in membership functions for CR and DS above the melting layer is mainly reflected by Z and Z_{DR}. In Figs. 5a and 5b, Z_{DR} is larger for CR, while Z is larger for DS and there is no difference in ρ_{hv} for CR and DS. Note that the Z_{DR} distribution for DS is slightly broader than the default membership functions, the range of Z_{DR} should be expanded appropriately. For the WS in the melting layer, all the dots in the Z–Z_{DR} are located within the area enclosed by red dashed lines, as shown in Fig. 5c. However, their distribution is broader than the area enclosed by the solid lines, which suggests that Z and Z_{DR} for WS are beyond the range specified by the membership functions with the value of 1. Meanwhile,

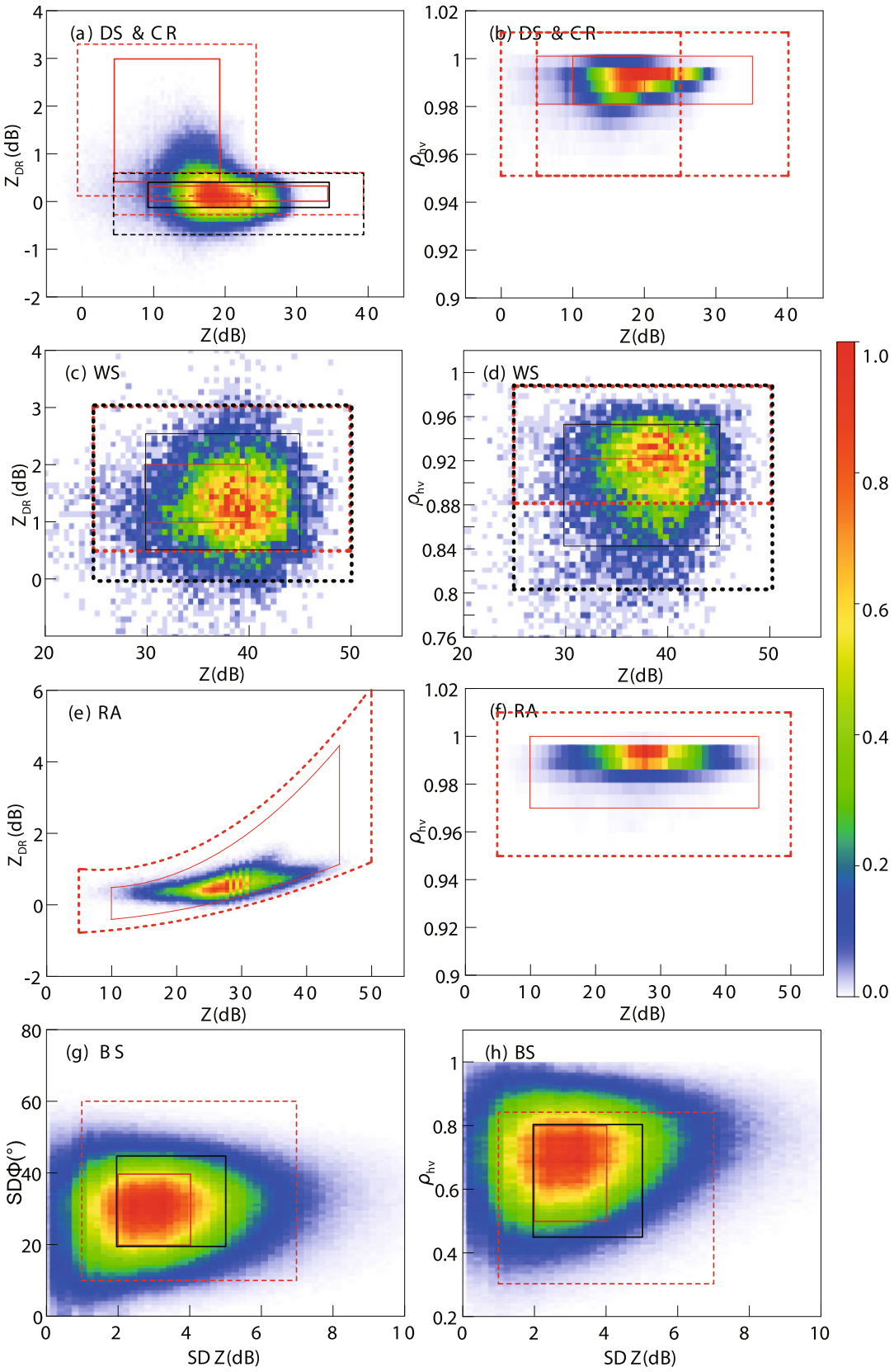

Fig. 5. Frequency distribution plots of polarimetric variables corresponding to various classes: (a) plot of Z–Z_{DR} for DS and CR; (b) plot of Z–ρ_{hv} for DS and CR; (c) plot of Z–Z_{DR} for WS; (d) plot of Z–ρ_{hv} for WS; (e) plot of Z–Z_{DR} for RA; (f) plot of Z–ρ_{hv} for RA; (g) plot of SD(Z)–SD(Φ_{DP}) for BS; (h) plot of SD(Z)–ρ_{hv} for BS. Red and black frames indicate the results with default and modified membership functions, respectively; solid lines represent the value where the membership function is 1, while dotted lines represent the value of 0.

the statistical value of ρ_{hv} in Fig. 5d for WS is obviously lower than the default value, many points located outside the areas enclosed by solid and dashed red lines. Thereby, the range of ρ_{hv} for WS can be expanded downwards. For the most commonly observed class of RA, the dots in the Z–Z_{DR} plots shown in Figs. 5e and 5f are located within the area enclosed by red solid lines, and the ρ_{hv} values are basically larger than 0.97, which are consistent with the default membership functions. For non-meteorological echoes, their distributions are basically matched with default membership functions, except that the scope of SD(Z), SD(Φ_{DP}) and ρ_{hv} is slightly wider, so subtle adjustment could be applied.

The above analysis indicates that it is unnecessary to modify the membership functions of Z for CR, DS and RA; the membership functions of Z_{DR} for CR and RA; and the membership functions of ρ_{hv} for CR, DS and RA. However, for DS, its Z_{DR} membership functions are changed from (−0.3, 0, 0.3, 0.6) to (−0.8, −0.2, 0.4, 0.6); and for WS, its Z membership functions are changed from (25, 30, 40, 50) to (25, 30, 45, 50), its Z_{DR} membership functions are changed from (0.5, 1, 2, 3) to (0, 0.5, 2.5, 3.0), and its ρ_{hv} membership functions are changed from (0.88, 0.92, 0.95, 0.985) to (0.8, 0.84, 0.95, 0.985). Furthermore, for BS, the SD(Z) membership functions are changed from (1, 2, 4, 7) to (1, 2, 5, 7), the SD(Φ_{DP}) membership functions are changed from (8, 10, 40, 60) to (8, 10, 45, 60), and the ρ_{hv} membership functions are changed from (0.3, 0.5, 0.8, 0.83) to (0.3, 0.45, 0.8, 0.83). All the modified membership functions are denoted by black lines in Fig. 5, which could basically contain all the statistical data.

Note that the statistical analysis in this section only considered the meteorological echoes of DS, WS, CR and RA in all the eight classes. For the class of HR, its membership functions are the same as that of RA, except the Z has a larger value and thus there is no need to modify its membership functions. In general, only three classes (GR, BD and RH) are not considered in the statistics. Due to a lack of approaches to extract hydrometeors of the above three classes from convective clouds, we surmise a practical way for echo extraction, which is based on the classical hydrometeor distribution from a "perfect" convection case where structures, circulations and microphysics processes can provide enough information. For example, hail is usually located within the echo overhang of a supercell, and its Z_{DR} is closed to 0 dB and its ρ_{hv} is also relatively lower (Kumjian and Ryzhkov, 2008; Johnson et al., 2016). BD are tightly linked with the phenomenon of "Z_{DR} column" in the vertical cross section (Illingworth et al., 1987; Brandes et al., 1995; Loney et al., 2002). These features could be manually discovered from typical cases, but no such case was found by Zhuhai radar in May 2014.

3.5. *Verification of the modified algorithm*

The confidence vectors Q for six input variables (Q_Z, Q_{ZDR}, $Q_{\rho_{hv}}$, Q_{KDP}, Q_{SDZ}, $Q_{SD\Phi}$) are obtained by multiplication of basic confidence functions (i.e., $Q(\Phi_{DP})$, Q(SNR), $Q(\rho_{hv})$ and $Q(dZ)$, $Q(dZ_{DR})$, $Q(d\Phi_{DP})$) with various combinations of thresholds. Since thresholds of SNR and ρ_{hv} are not sensitive for the variables of Z, K_{DP}, SD(Z) and SD(Φ_{DP}), the modification of Q(SNR) and $Q(\rho_{hv})$ will mainly affect Q_{ZDR} and $Q_{\rho_{hv}}$. Figure 6 shows the comparison between pre-modified and modified Q_{ZDR} and $Q_{\rho_{hv}}$ from Zhuhai radar measurements at 2320 LST 9 May 2014, and corresponding horizontal structures of SNR and ρ_{hv}, respectively.

This is a typical stratiform precipitation case. The ρ_{hv} structure shown in Fig. 6b shows a significant and homogeneous melting layer. On the edge of the echo structure, ρ_{hv} becomes weak due to the decrease in the SNR; to the west of Zhuhai station, precipitation almost stops and only non-meteorological echoes exist with very low ρ_{hv}. Comparing Figs. 6c and 6d with Figs. 6e and 6f, it is apparent that the confidence levels of Q_{ZDR} and $Q_{\rho_{hv}}$ with the default U.S. thresholds decreased to 0.6–0.7 due to the rapid decline of ρ_{hv} within the melting layer. Such weights cannot ensure the accuracy of the fuzzy logic computation for normal meteorological targets. After the modification, the confidence level maintains above 0.85. In Figs. 6c and 6e, there are no large changes in Q_{ZDR} and $Q_{\rho_{hv}}$ since the default threshold for SNR is small, which in fact cannot reflect the measurement errors under weak signals. After the modification, the confidence levels shown in Figs. 6d and 6f greatly decrease when SNR is lower, while values from non-meteorological echoes near the radar are still high, which ensures the effect of non-meteorological echo suppression.

Without the measurement of video sounding in clouds, we cannot directly inspect the modified classification results with real situations. However the vertical temperature profiles and hydrometeors near the ground could also reflect the particle distributions overhead, we can indirectly verify the effects of modifications based on comparison of the radar-detected spatial distribution of hydrometeors with soundings and surface observations near Zhuhai. Among these stations, Qiangyuan (station ID 59280) and Yangjiang (station ID 59663) are two L-band sounding radars close to Zhuhai. Sounding balloons are released daily at 0100, 0700, 1300 and 1900 LST to obtain temperature, pressure, humidity, wind speed, wind direction and altitude data at 1-s intervals. Plus, real-time surface observations and severe weather reports at national meteorological stations are also collected. Within the area covered by Zhuhai radar, there are 29 stations, and surface hail records are compared with the RH region from the HCA results.

Figure 7 presents the altitude of the melting layer detected by Zhuhai radar during 2200–2230 LST 9 May 2014 using the default and modified membership functions. To avoid the influence of radar beam broadening and interference, the upper and lower 20% of data points at each azimuth are excluded before the detection procedure, and the top and bottom of the melting layer are indicated by black solid lines. The results from using the default U.S. membership functions are presented in Fig. 7a, where the abnormal sparsity and uneven distribution of melted snowflakes lead to large fluctuations in the altitude at different azimuths. Since the melting layer corresponds to stable atmospheric stratification, this

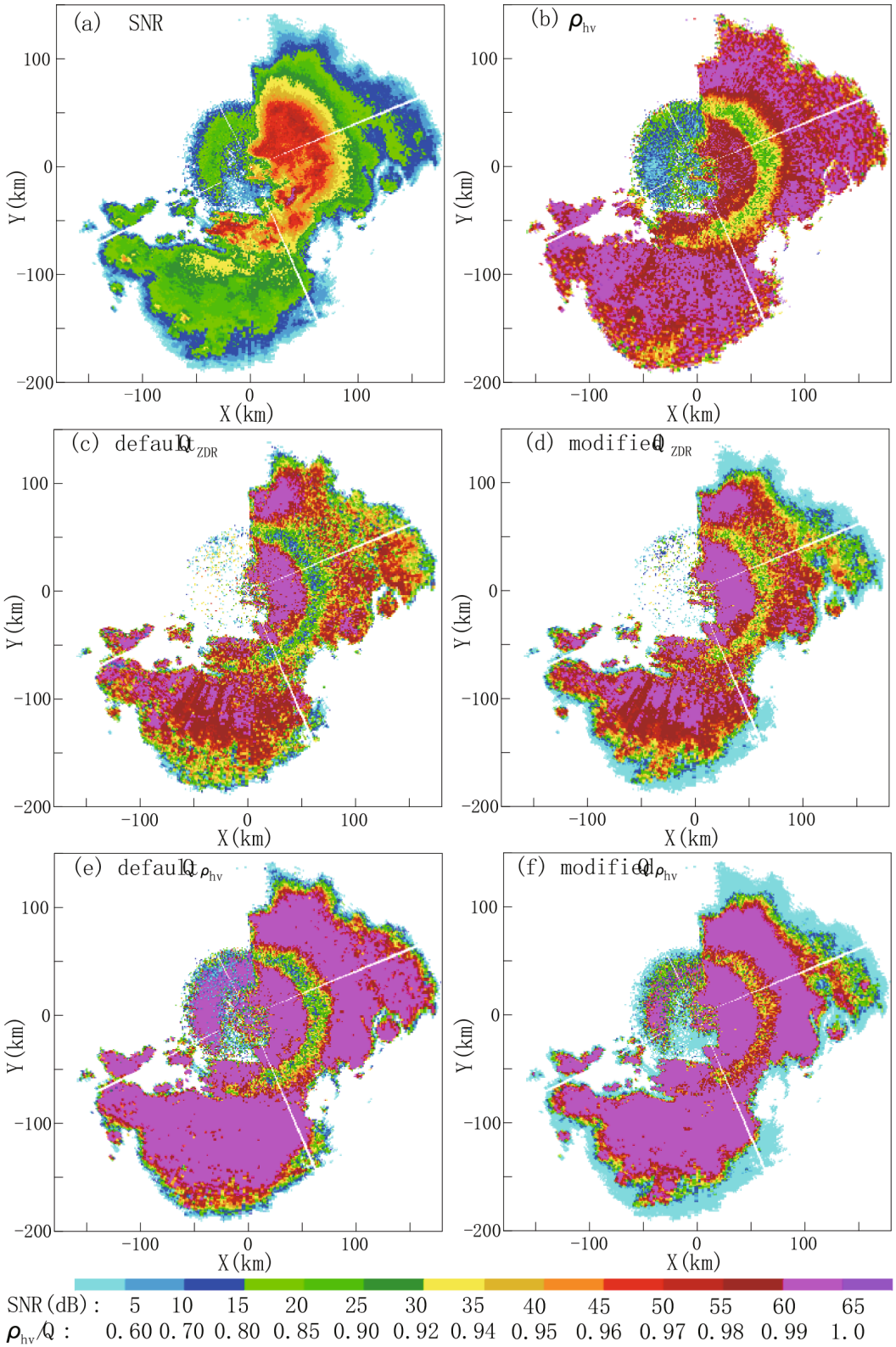

Fig. 6. The Plan Position Indicator (PPI) of SNR, ρ_{hv} and confidence at 3.3° elevation before and after the modification at 2320 LST 9 May 2014: (a) SNR; (b) ρ_{hv}; (c) default Q_{ZDR}; (d) modified Q_{ZDR}; (e) default $Q\rho_{hv}$; (f) modified $Q\rho_{hv}$.

phenomenon is apparently unreasonable. After modification of the membership functions, the concentration of melted snowflakes shown in Fig. 7b is about 2.5 times greater than in the previous results, and the spatial distribution becomes more homogeneous without any drastic fluctuations in azimuth. Therefore, with the modified membership functions,

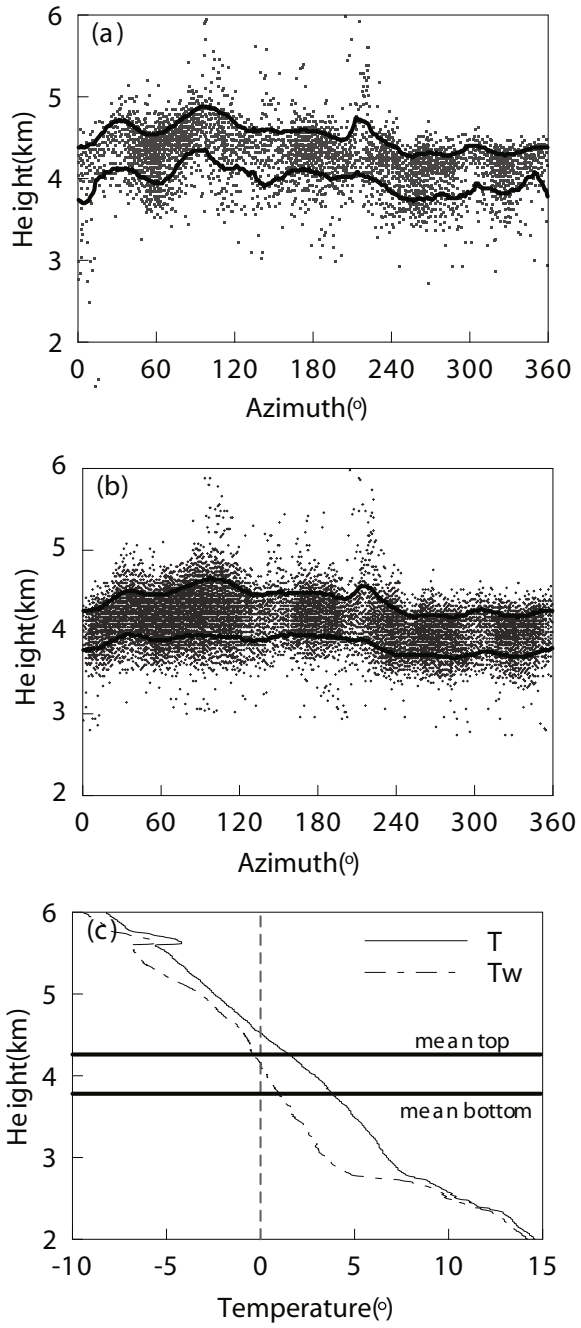

Fig. 7. Melting layer detected by radar using membership functions before and after the modification and its comparison with sounding data: (a) before modification; (b) after modification; (c) comparison of results after modification with sounding.

the HCA has better detection of WS in the melting layer. Figure 7c displays the temperature profile (solid line) from the sounding at 1848–1905 LST 9 May 2014 at Qingyuan station. Since the snow/ice melting is a kind of isobaric adiabatic process under the isentropic state, their melting level corresponds to the height where the dewpoint temperature (dotted line) is 0°C. Through comparison, the 0° dewpoint temperature from the sounding occurs at 4.16 km, and the radar-detected altitude of the melting layer top is about 4.26 km, which means they match very well. A similar result was also found in the study of Giangrande and Ryzhkov (2008) with the WSR-88D radar, indicating the results of the present study with the modified membership functions are reliable.

Next, observations of Zhuhai radar throughout May 2016 are used to verify the rationality of melting layer detection in the modified HCA, and Table 2 lists the comparison results of the melting layer altitude between Zhuhai radar and Qingyuan radiosonde. Only 10 sets of comparison results are presented in the table because the instances of stratiform precipitation detected by the radar did not completely match the time that sounding balloons were released at Qingyuan station. It is illustrated that the modified HCA performs well over a longer period, and the measurement error caused by sparse elevations is lower than 200 m. Similarly, Table 3 lists the detection results of the RH area from Zhuhai radar during May 2016, which is also verified by severe weather reports from nearby national weather stations. Although there are false-alarm situations, the HCA provides relatively reasonable warning information, with no obvious deficiency found. The reasons for the unavoidable false-alarm situations are discussed in detail in section 4.4.

4. Application of the localized HCA for a squall line in South China with microphysics analysis

During 1200–2000 LST 11 May 2014, a squall line generated along Enping–Zhaoqing of Guangdong and moved northeast to south. It eventually dissipated after reaching the Pearl River Delta. The localized HCA specialized for Zhuhai radar is applied to this squall line process to analyze the relationship between echo evolution and hydrometeor distributions. The microphysical processes during different stages of the squall line and the differences between radar-detected hail and surface observations are also discussed in this section.

Table 2. Comparison of melting layer altitude between Zhuhai radar and Qingyuan radiosonde in May 2016.

	Time (LST)									
	1400 8 May	2000 8 May	0700 9 May	1300 9 May	1900 9 May	0700 11 May	1900 11 May	1900 19 may	1300 20 May	1900 20 May
Sounding	4.28 km	4.44 km	4.45 km	4.23 km	4.16 km	4.69 km	4.83 km	4.84 km	4.95 km	4.41 km
Zhuhai	4.34 km	4.56 km	4.38 km	4.26 km	4.26 km	4.68 km	4.69 km	4.82 km	4.76 km	4.61 km

Table 3. Hail detection results of Zhuhai radar and verification by ground observations from nearby national weather stations in May 2016.

	Date			
	11 May	13 May	17 May	20 May
Weather station	3/26	1/28	3/26	2/27
Zhuhai radar	7/22	2/27	6/23	4/25
Hit	25	28	26	27
Miss	0	0	0	0
False alarm	4	1	3	2

4.1. *Synoptic background for the squall line development*

Analysis of the synoptic weather map (figure not shown) suggests that a trough at 500 hPa over the Yellow River Loop was gradually building at 0800 LST 10 May. The trough moved eastwards slowly due to the blocking of a high-pressure ridge over the Sea of Japan and gradually deepened. By 2000 LST 10 May 2014, the trough line extended southwards and eventually reached southern Hunan and northeastern Guangxi. Meanwhile, the subtropical high gradually intensified and moved northwards. The whole of Guangdong was located at the rear of the subtropical high and under the control of southwesterly winds from the surface to 700 hPa. Atmospheric moisture transport was significantly intensified, which is favorable for the development of convective instability. In addition, a wind shear between northerly and southerly winds developed above northeastern Guangxi at 2000 LST 10 May 2014 at 700 hPa. In the lower troposphere at 850–925 hPa, northerly and southerly winds converged with strong moisture convergence. At 0800 LST 11 May, the wind shear maintained and was moving southeastwards to the northern part of Guangdong. During 1400–2000 LST, the wind shear at 850–925 hPa reached Shenzhen of Guangdong, and further intensified to become a shear between northeasterly and southwesterly winds. The largest wind vector difference was close to 160° and wind speeds also increased, with the maximum wind speed close to 19 m s^{-1} at 700 hPa and 15 m s^{-1} at 850–925 hPa, indicating convection reached its climax. The strong wind shear in the lower air directly led to the squall line development.

According to the sounding data at Yangjiang station, the relative humidity was larger than 75% (maximum: 94%) in the layer below 700 hPa, rapidly decreased to 49% from 700 hPa to 650 hPa, and ultimately formed a distinct "upper-dry–low-wet" structure. Under the condition of strong vertical wind shear in the entire layer, this vertical wind field structure was favorable to the formation of a multi-cell squall line (Yu et al., 2008). Besides, Yangjiang station, as the nearest station to the hail area, showed in its skew-T log-P data that the convective available potential energy (CAPE) and convection inhibition (CIN) were only 214.8 and 108 J kg^{-1}, respectively, at 0200 11 May, and the instability was weak. However, at 0800 11 May, CAPE was 1846.1 J kg^{-1} and CIN was 10.2 J kg^{-1} (shown in Fig. 8a), indicating the instability increased sharply. As shown in Fig. 8b, at 1400 LST CAPE was up to 1942.0 J kg^{-1} and CIN was 7.0 J kg^{-1}, and the instability remained at a high level before the occurrence of hail. Meanwhile, the wind direction from the ground to the upper air rotated clockwise along with increasing altitude at 0800 LST (shown in Fig. 8c), and warm advection was obvious. While the wind direction in the upper atmosphere changed from west to southwest at 1400 LST (shown in Fig. 8d), the wind speed increased by 5 m s^{-1} (equivalent to one point on the Beaufort scale), and warm advection further strengthened. This provided suitable conditions for the development of strong convective weather.

4.2. *Evolution of hydrometeor distributions during the squall line development*

Observations and HCA results from Zhuhai radar for 1030–1800 LST 11 May are utilized to analyze the life cycle of the squall line; the horizontal and vertical structures are presented in Figs. 9 and 10, respectively. Furthermore, three statistical parameters are also defined for quantitative analysis: maximum Z (Z_{max}); area of Z larger than 45 dBZ (A_Z); and area of RH (A_{RH}) identified by the HCA.

At 1030 LST of the squall line initiation, several small-scale convective cells appear near Enping of Guangdong province. Under the condition of convective instability, these cells develop rapidly and transform into cumulonimbus monomers with horizontal scales of ~20 km (shown in Fig. 9a). The monomer along 112.1°–112.4°E is relatively large and develops rigorously, where Z_{max} reaches 53 dBZ and A_Z is ~178.3 km^2. In the vertical direction, the echo top reaches 14 km and GR is detected within the height of 5–10 km, which melts when falling below 4 km, resulting in heavy rainfall. One hour later, at 1228 LST, the cumulonimbus monomer further develops and new cells form over large areas to the east of the leading edge. As shown in Fig. 9b, an echo belt of about 80 km in length occurs with a Z_{max} of 57 dBZ, and the A_Z increases to 681.1 km^2, which is 3.8 times the amount one hour beforehand. The area of GR in the middle and upper troposphere also increases significantly after the echo top reaches 15 km, and the results of the classification indicate that a discontinuous RH area with an A_{RH} of 22.6 km^2 exists. Meanwhile, hail is observed at Taishan national station (22.15°N, 112.47°E). Only 40 min later, as shown in Fig. 9c, the previous and newly-generated cells merge with one another, forming a bow echo of about 150 km in length. At this time, the A_Z and A_{RH} increase to 1109.7 km^2 and 40.1 km^2, which are twofold larger than their previous values. Although the RH can be identified by the HCA over a large area, its spatial distribution is still unorganized and is widely located in the center of the bow echo. The configuration of the squall line is established at 1325 LST, when the convection also reaches its first peak. As shown in Fig. 9d, convective clouds develop rigorously and keep triggering new cells in front of the moving direction. The major RH region is more concentrated at this time, which follows the leading edge of the bow echo and moves eastwards. Comparing the observations at 1254 and 1335 LST, the Z_{max} and A_Z

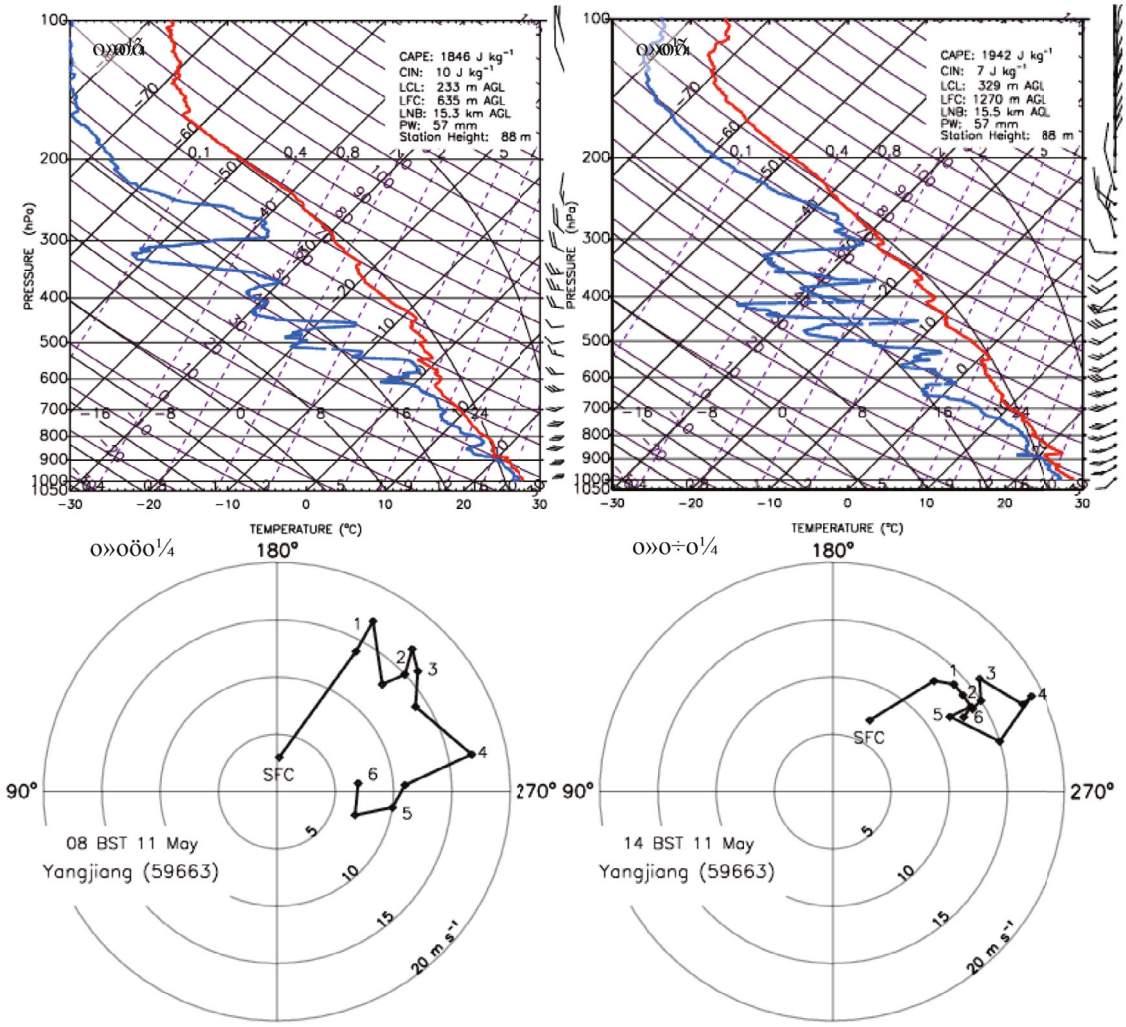

Fig. 8. (a, b) Skew-T log-P plots of sounding from Yangjiang station at 0800 and 1400 LST 11 May 2014 and (c, d) corresponding hodographs of horizontal wind vectors.

are basically consistent, while the A_{RH} detected by the HCA increases by 344% to 138.2 km^2, suggesting the strongest convection. No hail is observed at the surface due to the RH area being concentrated over the Pearl River estuary.

In the following 30 min, the northeastern part of the squall line develops rapidly, but the southwestern part develops slowly, leading to a split in the squall line. As shown in Fig. 9e, the eastern part continues to move eastwards and weakens at 1412 LST. The echo length decreases to 60 km, the A_Z and A_{RH} are only 59.4% and 22.1%, respectively, of their amounts 30 min previously, and they keep on decreasing at later times. WS particles are found in the northeastern region in the results of the HCA at 1500 LST, suggesting that some convective clouds have dissipated and stratiform clouds are developing (Figs. 9f–h). For the southwestern part, two echo belts are shown in Fig. 9e at 1412 LST. The first echo belt, belonging to the previous squall line, develops slowly on a small scale and splits into multiple cells. The Z_{max} is lower than 50 dBZ; only raindrops are detected from the results of the HCA at the lower levels. At the rear of the first echo belt, the second echo belt develops rapidly towards the east. The vertical structures are shown in Fig. 10a, in which the first convective belt in the front is weak and its echo top is only at 5 km. GR originally located in the mid-troposphere almost completely disappears due to the weakened convection. At 10 km behind the weak monomer, the top of the newly generated clouds reaches above 8 km, and GR also appears at 5–8 km. Most of the GR melts into rain or HR as it falls below freezing level, and RH areas are seldom observed in the lower troposphere. This situation lasts for 30 mins until 1443 LST when the two cells merge (Fig. 9f). During this process, no sporadic RH area is observed, and no significant increases in A_Z is found. However, the area of GR in the vertical structure clearly increases, which implies that the monomer further intensifies (Fig. 10b).

After merging, the monomer develops rapidly, and the configuration of the squall line is established again at 1504 LST, where the bow echo length in Fig. 9g—extending from Jiangmen to Zhongshan and Shenzhen—is about 140 km. The Z_{max} reaches 60 dBZ and the A_Z increases to 917.7 km^2,

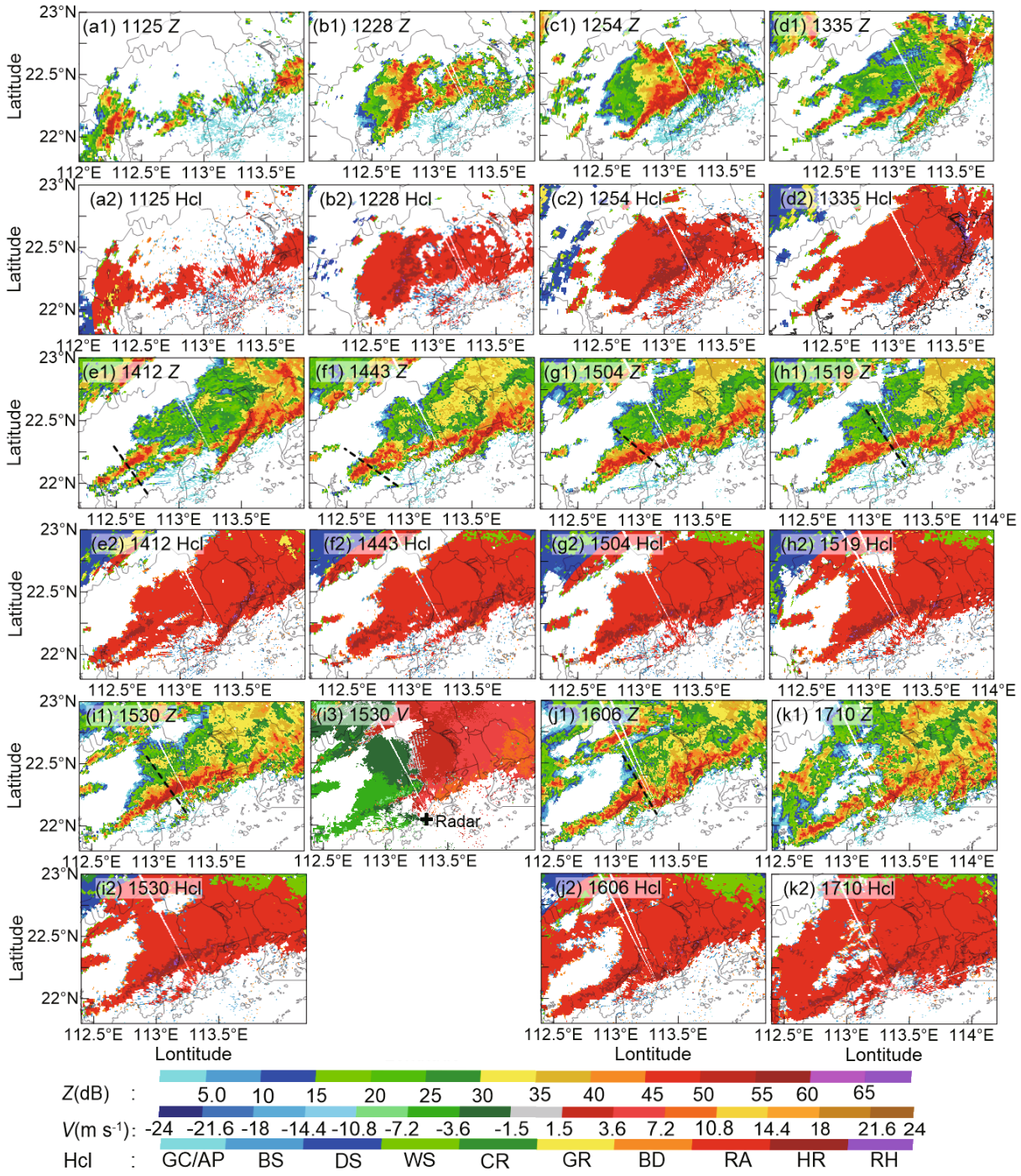

Fig. 9. Horizontal distributions of Z, V, and results of classification at 1.4° elevation. Black dotted lines denote the location of the cross section in Fig. 10.

but the classes of RA and HR still occupy an overall majority in the HCA results and no significant RH region can be detected. The radial cross sections in Fig. 10c clearly show that the core location of the squall line corresponds to the V convergence region at 0–4 km altitude. At 8 km above the melting layer, supercooled water droplets and ice crystals collide and stick together, and form GR where Z is higher than the CR, while its ρ_{hv} is conversely lower. Since the convective monomers still do not reach their climax, this GR mostly melts into raindrops below the freezing level. In the following 30 min, although the Z_{max} and A_Z are similar to those at 1504 LST, the A_{RH} keeps increasing. As shown in the radial cross sections at 1519 LST in Fig. 10d, the top of some convective monomers reaches altitudes above 15 km, and the V convergence can occur at a height of 6 km, indicating there are not only much stronger updrafts but also repetitive colli-

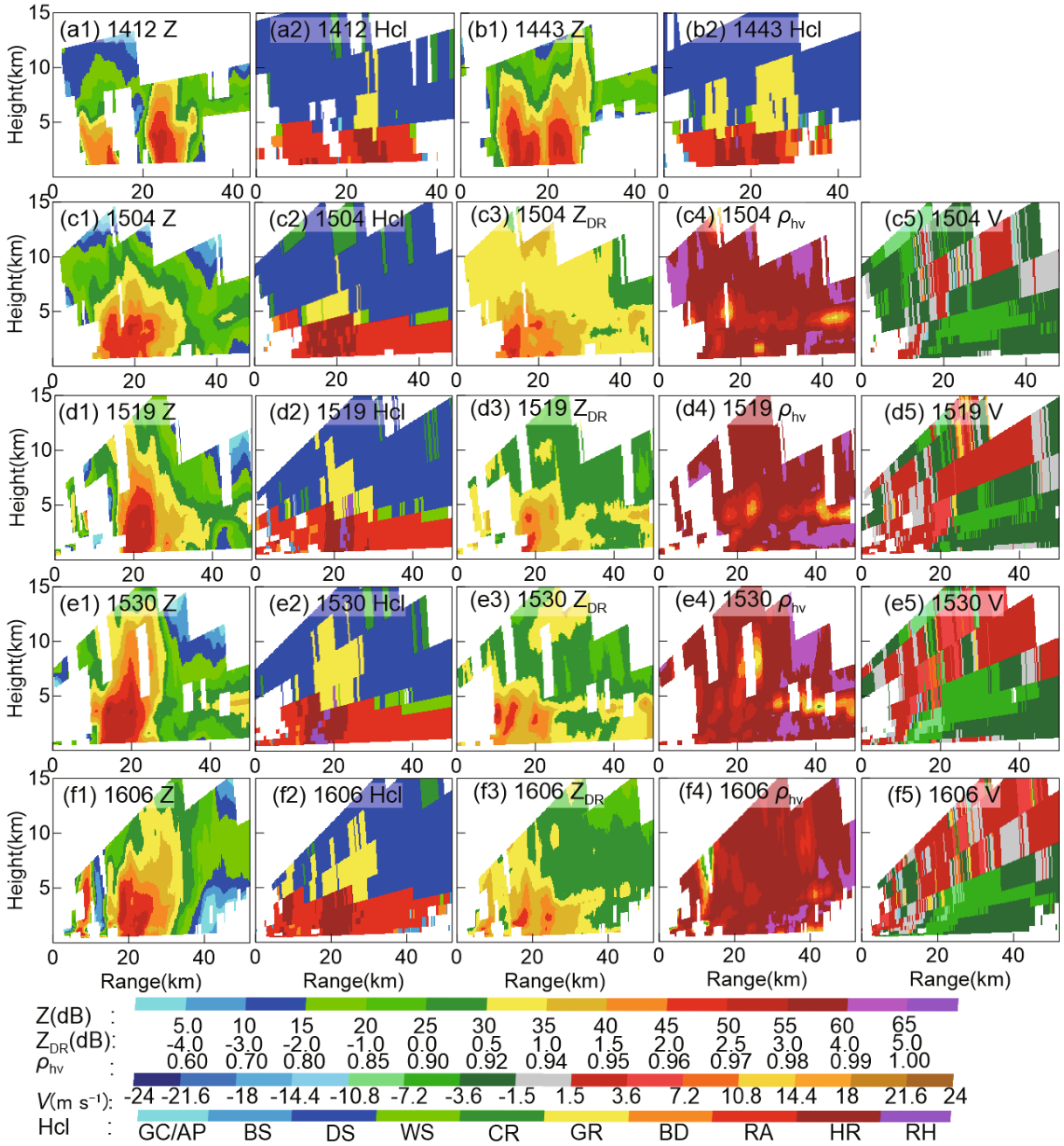

Fig. 10. Vertical structures along the radial direction of the polarimetric variables and results of hydrometeor classification for Zhuhai radar measurement.

sion between GR and supercooled water droplets in clouds. This GR behaves as hail embryos, leading to the formation of the RH layer below.

The maximum A_{RH} of 36.6 km^2 at this stage appears at 1530, when the squall line reaches its second peak. The V shown in Fig. 9i indicates a distinct convergence region corresponding to the bow echo. Mid-level convergence can be found from elevations of 2° to 6° corresponding to strong upward motions within the squall line. A 5-km-wide RH region appears in the vertical structure shown in Fig. 10e. Compared with the polarimetric variables at this time, it is found that there is no big difference in Z between the HR caused by melting GR and RH. However, the deformation of raindrops during their descent results in larger Z_{DR} and ρ_{hv}, while the Z_{DR} in the hail region is relatively lower at more than 0.5 dB and the ρ_{hv} is also lower because of the melting particles. The above differences make the HCA results completely different. At 1606 LST, the echo top, V, and regions of GR and RH from the convergence zone all obviously decrease (Fig. 10f). At the altitude of 4.5 km in Figs. 10e and d, Z and Z_{DR} in the rear of the echo core are distinctly larger, and the ρ_{hv} is opposite. Based on the HCA results, WS particles appear

in this region, which corresponds to stratiform precipitation after the dissipation of convective clouds of the squall line.

During the development of this squall line, the RH region identified by the HCA is always located in front of the leading edge of the bow echo corresponding to a composite Z larger than 50 dBZ, an echo top higher than 10 km, and its Z_{DR} also being lower from around the rain region. Moreover, the evolution of A_{RH} is consistent with the Z_{max}, A_Z and surface observations, while the A_{RH} is more significant for the strengthening and weakening of the life cycle of convective clouds. These results indicate that the HCA can realistically reflect changes in the squall line intensity during its development, and thus provide helpful information for nowcasting.

4.3. *Kinematic and microphysical analysis at different stages of the squall line*

As discussed previously, the newly formed convective cells in the southwestern part along (22.0°–22.2°N, 112.4°–112.7°E) rapidly develop and eventually form a squall line with a length of ~100 km during 1412–1530 LST. Under the premise of sufficient representativeness, the evolution of the squall line is divided into four stages: the onset stage of small-scale cells (S1; 1401–1412 LST; 22.0°–22.2°N, 112.4°–112.7°E); the developing and intensification stage of convective cells (S2; 1438–1448 LST; 22.0°–22.2°N, 112.7°–113.0°E); the maturing stage and formation of the squall line (S3; 1525–1530 LST; 22.15°–22.35°N, 113.0°–113.3°E); and the dissipating stage with stratiform clouds (S4; 1659–1710 LST; 22.35°–22.55°N, 113.2°–113.5°E). To investigate the kinematic and microphysical structures, contoured frequency by altitude diagrams (CFADs) of Z, Z_{DR}, K_{DP} and vertical velocity (w) are presented in Fig. 11. Herein, the 3D wind fields are retrieved from Guangzhou and Shenzhen radar data using the NCAR's Custom Editing and Display of Reduced Information in Cartesian Space package (Mohr et al., 1986). The temporal and spatial resolutions of the retrieved wind field are 6 min and 1.0 km in the horizontal direction and 0.5 km in the vertical direction, respectively. By contrast with the CFADs, the proportions of each hydrometeor class changing with altitude are counted in Fig. 11.

During S1, the distribution of Z is from 30 to 50 dBZ (Fig. 11a) at the lower level, and Z_{DR} is from 0.5 to 1.5 dB (Fig. 11f), both revealing features of large raindrops. With the height increasing, Z and Z_{DR} decrease rapidly, and only small-sized raindrops are found at the altitude of 3.5 km. Above the freezing level where the altitude is 5–7 km, the temperature is −5°C to −15°, Z is between 20 and 40 dBZ, and Z_{DR} is between 0.8 and 1 dB, we surmise that the cloud is dominated by supercooled water droplets for the relatively large Z_{DR}. For higher levels where the temperature is lower than −15°, Z_{DR} is relatively small, at around 0 dB, associated with the features of DS and CR. From the lower to upper troposphere, K_{DP}, which remains small, represents a limited water content (Fig. 11k). In the dual-Doppler analyses of the convective cells (Fig. 11p), the distribution of w is concentrated in a small area from −3 to 3 m s^{-1}, with the maximum w of 3 m s^{-1} at the height of 4 km. It is proved that updrafts and downdrafts are not strong during initial stage. The result of the HCA (Fig. 11u) is also consistent with the above analysis. Raindrops (RA and HR) occupy the largest proportion below the freezing level, and the number of frozen precipitation particles (GR or RH) is relatively small due to the weak updrafts.

With the development of convections, Z and K_{DP} at different levels are both intensified during S2 (Figs. 11b and l). From the ground to the height of 4 km, Z and Z_{DR} are 40–50 dBZ and 1–2 dB, respectively, and K_{DP} is increased to 2° km^{-1}, corresponding to the large-sized raindrops with higher water content. At the altitude of 7 km above freezing level, the maximum Z reaches 45 dBZ, which is beyond the normal distribution of CR and DS. Meanwhile, Z_{DR} at the same height decreases to 0.5 dB. The increased Z and decreased Z_{DR} confirm the existence of spherical GR. The larger variance of w in Fig. 11q exhibits enhanced updrafts and downdrafts. The maximum and mean w reach 14 and 2.7 m s^{-1}, respectively, at the height of 8 km, both having increased substantially. The fact that the dominant microphysical process at this level is mainly the collection of CR and supercooled water droplets carried by updrafts, results in the generation and growth of GR, which also plays a key role in hail formation (Hong et al., 2002). Due to the strong updrafts, the proportion of GR at the altitude of 5 km triples in the space of 30 min (Fig. 11v), with most melting into HR below the freezing level. Also, only a small proportion of RH is identified by the HCA.

During the mature stage, the original isolated convective cells combine and form the squall line. The kinematic and polarimetric characteristics at this time indicate that convections reach their peak intensity. The altitude of CR with small Z (Fig. 11c) and moderate Z_{DR} (Fig. 11h) is higher than 13 km, GR with moderate Z and small Z_{DR} appears from 6 to 10 km, both having increased from previous stages. Under the freezing level, Z and K_{DP} (Fig. 11m) greatly increase to 50–60 dBZ and 4° km^{-1}, respectively, while Z_{DR} is almost unchanged and ρ_{hv} (figure not shown) decreases to 0.94–0.99. We surmise the reason for this phenomenon is the mixture of hail and big raindrops. From the CFAD of w in Fig. 11r, the maximum w exceeds 15 m s^{-1}, and the mean w almost doubles again and reaches 4.81 m s^{-1} at the height of 8.5 km, suggesting very strong vertical motion can support the growth of hail. When hail with huge Z and small Z_{DR}, and big raindrops with large Z and large Z_{DR}, are simultaneously detected by Zhuhai radar, Z will increase, Z_{DR} will remain or decline depending on the proportion of hail, and ρ_{hv} will be kept at a lower value due to the sustained melting of hail. In fact, the proportion of RH is lower than 20% in Fig. 11w, and the class of HR is the dominant hydrometeor. For stratiform clouds during S4, only weak updrafts and downdrafts are found in Fig. 11s. The Z (Fig. 11d) and Z_{DR} (Fig. 11i) have dropped significantly, and the K_{DP} (Fig. 11n) is less than 0.5° km^{-1}, which is one eighth of that during S3, indicating that only small raindrops with low water content exist. It is clear that, without the support of updrafts, the size of raindrops could not grow to a sufficiently large enough size to

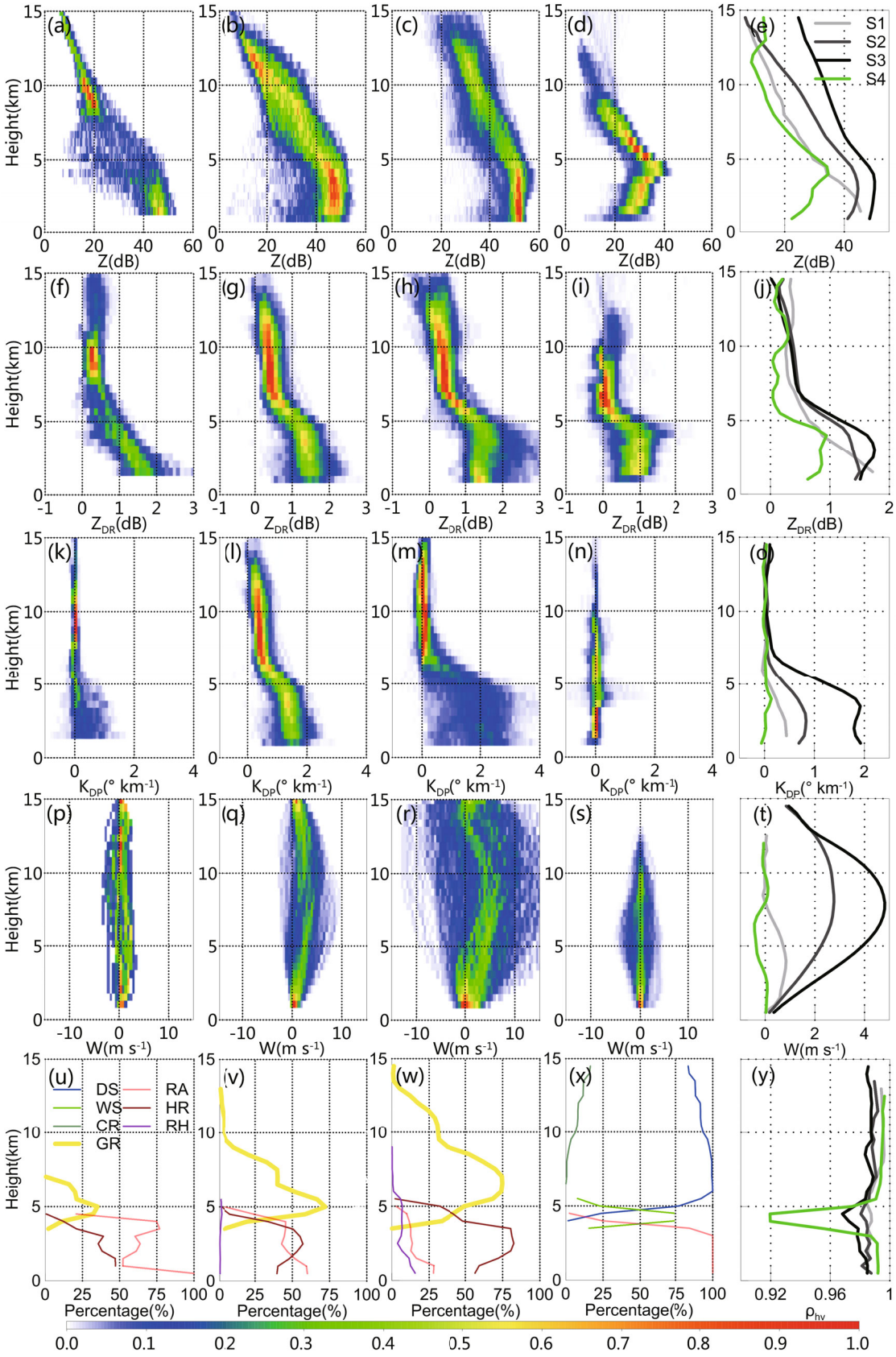

Fig. 11. CFADs of the Z data during four stages of development: (a) onset stage of small-scale cells (S1); (b) developing and intensification stage of convective cells (S2); (c) maturing stage and formation of the squall line (S3); (d) dissipating stage with stratiform clouds (S4). (e) Averaged profiles of Z from the four stages. (f–j) As in Figs. 10a–e but for Z_{DR}. (k–o) As in Figs. 10a–e but for K_{DP}. (p–t) As in Figs. 10a–e but for w. (u–x) Proportions of each hydrometeor class changing with altitude during the four stages. (y) As in Fig. 10e but for ρ_{hv}.

fall to the ground.

The mean vertical profiles of Z (Fig. 11e), Z_{DR} (Fig. 11j), K_{DP} (Fig. 11o), w (Fig. 11t) and ρ_{hv} (Fig. 11y) are also calculated to investigate the vertical kinematic and microphysical structures. With the development of this squall line, the w keeps increasing from S1 to S3, corresponding to higher Z, Z_{DR} and K_{DP}. That means the raindrops have a longer time to grow, and GR and RH have also generated in convective cells. In the stratiform precipitation of S4, the negative value of mean w, and rapidly decreasing Z, Z_{DR} and K_{DP}, indicate the dissipation of convective cells. At the height of the freezing level, the signature of melting particles is clear where Z and Z_{DR} are larger than those of adjacent levels; meanwhile, ρ_{hv} is smaller. Note that the primary melting particles within convective clouds are GR and RH, while in stratiform clouds they are WS. Below the freezing level, ρ_{hv} in S3 increases downwards to the ground, representing the gradual thawing of RH and GR from the height of 5 km. As the low-level temperature of South China reached a higher degree on 9 May, small-sized hail and GR with lower ρ_{hv} would have completely melted into raindrops with higher ρ_{hv} before they reached the ground. With the proportion of hail and GR decreasing, the Z_{DR} enhances correspondingly. In contrast with the ρ_{hv} value of 0.995 from stratiform precipitation, the ρ_{hv} from the squall line during S3 rises to 0.98 near the surface, so we surmise that part of the hail, with relatively large size, can fall to the ground.

We noticed that the mean Z_{DR} observed by Zhuhai radar is almost constant and close to 0 above the altitude of 8.8 km, where temperature is −20°C, from S1 to S4. According to the research of Bailey and Hallett (2009) and Wang et al. (2014), CR tend to grow slowly, with regular shapes, due to the limited ice supersaturation, which results in a large Z_{DR}. With the augmentation of supersaturation, more irregular shapes of CR can be found. Considering the plentiful moisture content of South China and the intense updrafts of the squall line, more water vapor is transported to the upper troposphere, and the CR would grow faster with more irregular shapes, causing the decreasing of Z_{DR}.

4.4. *Comparison of radar-detected hail regions and surface observations*

As discussed in section 3.5, the localized HCA performs well over a longer period, and reasonable warning information could be obtained despite some false alarms. To evaluate the reliability of the HCA in detail during this squall line case, Fig. 12 compares the radar-detected RH regions and surface observations. Considering that the minimum detectable altitude of radar increases with radial distance, different colors are used to denote the height of the RH region according to its position in each layer, and stations with hail reports are denoted by triangles. Among the twenty-nine meteorological stations near Zhuhai radar, three of them observed the hail. By contrast, seven stations are located within the RH region, while twenty-two are outside the region.

At the three stations where hail is observed, i.e., Doumen (ID 59487), Taishan (ID 59478) and Nanhai (ID 59288), Doumen is only 23 km away from Zhuhai radar. A small amount of RH is found in the second and third layers, while no hail is detected in the first elevation due to the influence of the cone of silence and ground clutter. Around Taishan station, which is located 93 km to the west of Zhuhai radar, the RH is visible in the first layer. For the nearby stations of Enping (ID 59477), Kaiping (ID 59475) and Heshan (ID 59473), no RH is detected. The results of the HCA are completely consistent with observations at these meteorological stations. Note that Nanhai station (23.09°N, 113.01°E), which is 123 km away from Zhuhai radar, is not located on the moving path of this squall line. Instead, a local convective cell passed over this region during 1430–1450 LST. A sporadic RH region is subtly observed in the results of the HCA, and hail is also observed at the surface. However, a small area of RH also covers Huadu (ID 59284), which is located to the northeast of Nanhai, and no hail is reported. Considering that

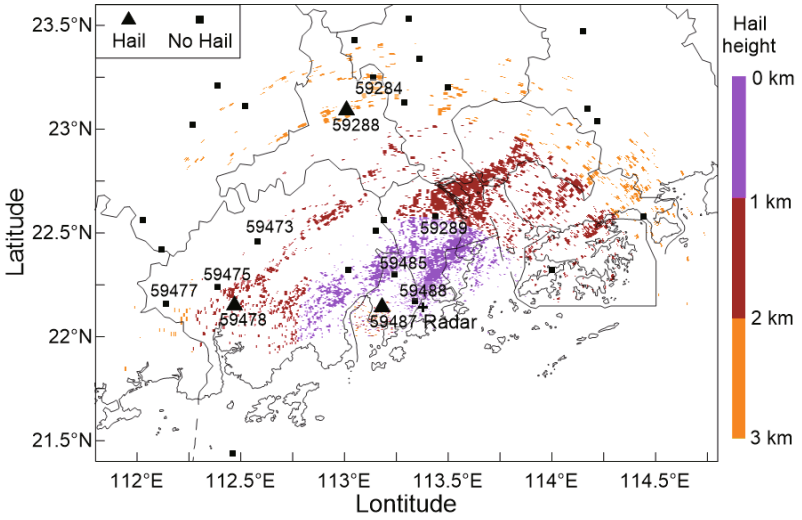

Fig. 12. Hail detection at various heights and comparison with surface observations.

the height of the radar beam at 0.5° elevation is about 2.2 km after propagation of 123 km, some small-sized hail may have melted before falling to the ground.

The other three stations where the altitude of the radar-detected RH regions is lower than 2 km without surface observations, are Zhuhai (ID 59488), near the radar; Zhongshan (ID 59487), 33 km to the northwest of the radar; and Donguan (ID 59289), 61 km to the northeast of the radar. Among these three stations, Zhongshan is located at the edge of this squall line. The average wind speed at 2-min intervals at the corresponding time is only 3.5 m s^{-1}, and hourly precipitation is only 5.9 mm. Results indicate that the convection is weak at Zhongshan station, and the hail density is relatively low. This hail may have melted during its fall or has yet to fall near the station. Zhuhai is also located at the edge of the RH region, but the overhead convection is sufficiently strong. So, when the squall line is passing through, instantaneous and 2-min-averaged wind speeds reach 11.3 m s^{-1} and 8.2 m s^{-1}, respectively, and hourly precipitation reaches 26 mm, 26.2 mm and 55.5 mm during the three-hour period. Thereby, it is possible that hail did not exist near the station, or it at least did not exist during the observational period of the station. A similar situation was also found at Dongguan station, where large areas of RH were detected by the radar, but no hail reports were recorded at the ground. Moreover, other meteorological elements such as temperature and precipitation are also missing during the 30-min period of the strongest convection. We surmise that the missing measurement caused the false alarm of the HCA at Dongguan station.

5. Conclusions and discussion

In this study, a HCA is developed based on the U.S. operational algorithm and the methodology of statistics-based optimization is also proposed. Then, this localized algorithm is utilized for analysis of a squall line process in South China. The major conclusions are as follows:

(1) A reasonable calibration procedure has been applied to Zhuhai radar, and the systematic bias of Z_{DR} has been corrected. The reliability of Zhuhai radar measurements deteriorates when the SNR is lower than 20 dB, and the ρ_{hv} within the melting layer is usually lower than that of the U.S. WSR-88D radar. Considering the difference in the radar hardware and the DSD over South China, the default parameters used in the U.S. algorithm cannot be directly applied for Zhuhai radar measurements.

(2) The membership functions used in the HCA for DS, WS, CR, and BS are optimized based on the statistical analysis of polarimetric variables from raindrops, snow and ice crystals, melting particles, and non-meteorological echoes. Also, the thresholds of Z_{DR} and ρ_{hv} for confidence vector computation are modified based on actual data quality of Zhuhai radar. After obtaining the localized HCA especially for Zhuhai, the rationality of the above modifications is verified against sounding and surface observations, and it performs well over a one-month test.

(3) The localized HCA is applied to a squall line case on 11 May 2014. The horizontal and vertical structures indicate that the algorithm can provide reasonable details, and the results of the HCA—especially the RH region—can reflect the life cycle of the squall line. Besides, the analysis of kinematic and microphysical fields is also highly consistent with the HCA results.

(4) Comparisons between the RH regions detected by Zhuhai radar and surface observations collected by national meteorological stations suggest that the warning information provided by the HCA is reasonably accurate. Among the 29 stations, radar detections are consistent with observations at 25 stations. False alarms seem inevitable due to the minimum radar-detectable altitude and the manual observation limit.

Only the area of the RH is produced by the HCA in this study, whereas the hail size and density in this region remain unknown. Similarly, weather observers cannot observe and record weather phenomena all the time since they also need to upload observations and maintain instruments, amongst other tasks. Thereby, during the limited observational period, it is uncertain whether hail was large enough to reach the ground before it completely melted. It is also unknown whether the density of hail reaching the surface was high enough to be observed in time. These issues all need further study. In subsequent research, we will apply the algorithm for other dual-polarization radars that have been put into trial operation in South China. The algorithm will be further evaluated, which will lay a solid foundation for the development of HCAs specifically suitable for Chinese radar hardware and precipitation characteristics.

Acknowledgements. This work was jointly funded by the National Natural Science Foundation of China (Grant Nos. 41675023, 91337103, 91437101 and 41675029) the Scientific Research Projects of CAMS (Grant Nos. 2016Z005 and 2016LASW-B12), and the Postgraduate Research & Practice Innovation Program of Jiangsu Province (Grant Nos. KYCX17_0880). Thanks to Xi Liu and Di Liu at Nanjing University of Information Science and Technology, China, for their help with the English and for their suggestions regarding data processing.

REFERENCES

Bailey, M. P., and J. Hallett, 2009: A comprehensive habit diagram for atmospheric ice crystals: confirmation from the laboratory, AIRS II, and other field studies. *J. Atmos. Sci.*, **66**, 2888–2899, https://doi.org/10.1175/2009JAS2883.1.

Brandes, E. A., J. Vivekanandan, J. D. Tuttle, and C. J. Kessinger, 1995: A study of thunderstorm microphysics with multiparameter radar and aircraft observations. *Mon. Wea. Rev.*, **123**, 3129–3143, https://doi.org/10.1175/1520-0493(1995)123<3129:ASOTMW>2.0.CO;2.

Chen, X. C., F. G. Zhang, and K. Zhao, 2016: Diurnal variations of the Land–sea breeze and its related precipitation over South China. *J. Atmos. Sci.*, **73**, 4793–4815, https://doi.org/10.1175/JAS-D-16-0106.1.

Chen, X. C., K. Zhao, and M. Xue, 2014: Spatial and temporal

characteristics of warm season convection over Pearl River Delta region, China, based on 3 years of operational radar data. *J. Geophys. Res.*, **119**, 12 447–12 465, https://doi.org/10.1002/2014JD021965.

Chen, X. C., K. Zhao, M. Xue, B. W. Zhou, X. X. Huang, and W. X. Xu, 2015: Radar observed diurnal cycle and propagation of convection over the Pearl River Delta during Mei-Yu season. *J. Geophys. Res. Atmos.*, **120**, 12 557–12 575, https://doi.org/10.1002/2015JD023872.

Elmore, K. L., 2011: The NSSL hydrometeor classification algorithm in winter surface precipitation: Evaluation and future development. *Wea. Forecasting*, **26**, 756–765, https://doi.org/10.1175/WAF-D-10-05011.1.

Giangrande, S. E., and A. V. Ryzhkov, 2005: Calibration of dualpolarization radar in the presence of partial beam blockage. *J. Atmos. Oceanic Technol.*, **22**, 1156–1166, https://doi.org/10.1175/JTECH1766.1.

Giangrande, S. E., and A. V. Ryzhkov, 2008: Estimation of rainfall based on the results of polarimetric echo classification. *J. Appl. Meteor. Climatol.*, **47**, 2445–2462, https://doi.org/10.1175/2008JAMC1753.1.

Heinselman, P. L., and A. V. Ryzhkov, 2006: Validation of polarimetric hail detection. *Wea. Forecasting*, **21**, 839–850, https://doi.org/10.1175/WAF956.1.

Hong, Y. C., H. Xiao, H. Y. Li, and Z. X. Hu, 2002: Studies on microphysical processes in hail cloud. *Chinese Journal of Atmospheric Sciences*, **26**, 421–432, https://doi.org/10.3878/j.issn.1006-9895.2002.03.13. (in Chinese)

Hu, Z. Q., L. P. Liu, and L. L. Wu, 2014: Comparison among several system biases calibration methods on c-band polarimetric radar. *Plateau Meteorology*, **33**, 104–107. (in Chinese)

Hu, Z. Q., L. P. Liu, L. L. Wu, and Q. Wei, 2015: A comparison of de-noising methods for differential phase shift and associated rainfall estimation. *J. Meteor. Res.*, **29**, 315–327, https://doi.org/10.1007/s13351-015-4062-6.

Illingworth, A. J., J. W. F. Goddard, and S. M. Cherry, 1987: Polarization radar studies of precipitation development in convective storms. *Quart. J. Roy. Meteor. Soc.*, **113**, 469–489, https://doi.org/10.1002/qj.49711347604.

Jameson, A. R., M. L. Larsen, and A. B. Kostinski, 2015: On the variability of drop size distributions over areas. *J. Atmos. Sci.*, **72**, 1386–1397, https://doi.org/10.1175/JAS-D-14-0258.1.

Jameson, A. R., 2016: Quantifying drop size distribution variability over areas: Some implications for ground validation experiments. *Journal of Hydrometeorology*, **17**, 2689–2698, https://doi.org/10.1175/JHM-D-16-0094.1.

Johnson, M., Y. Jung, D. T. Dawson, and M. Xue, 2016: Comparison of simulated polarimetric signatures in idealized supercell storms using two-moment bulk microphysics schemes in WRF. *Mon. Wea. Rev.*, **144**, 971–996, https://doi.org/10.1175/MWR-D-15-0233.1.

Kumjian, M. R., and A. V. Ryzhkov, 2008: Polarimetric signatures in supercell thunderstorms. *J. Appl. Meteor. Climatol.*, **47**, 1940–1961, https://doi.org/10.1175/2007JAMC1874.1.

Lim, S., V. Chandrasekar, and V. N. Bringi, 2005: Hydrometeor classification system using dual-polarization radar measurements: Model improvements and in situ verification. *IEEE Trans. Geosci. Remote Sens.*, **43**, 792–801, https://doi.org/10.1109/TGRS.2004.843077.

Liu, H., and V. Chandrasekar, 2000: Classification of hydrometeors based on polarimetric radar measurements: Development of fuzzy logic and neuro-fuzzy systems, and in situ verification. *J. Atmos. Oceanic Technol.*, **17**, 140–164, https://doi.org/10.1175/1520-0426(2000)017<0140:COHBOP>2.0.CO;2.

Liu, L. P., B. X. Xu, Z. J. Wang, and J. Wang, 1992: Study of Hail with C–B and dual linear polarization radar. *Chinese Journal of Atmospheric Sciences*, **16**, 370–376. (in Chinese)

Liu, L. P., Y. F. Qian, Z. J. Wang, and R. Z. Chu, 1996: Comparative study on dual linear polarization radar measuring rainfall rate. *Chinese Journal of Atmospheric Sciences*, **20**, 615–619, https://doi.org/10.3878/j.issn.1006-9895.1996.05.13. (in Chinese)

Liu, L. P., Z. Q. Hu, and C. Wu, 2016: Development and application of dual linear polarization radar and phased-array radar. *Advances in Meteorological Science and Technology*, **6**, 28–33. (in Chinese)

Liu, Y. N., X. Xiao, Z. D. Yao, and L. Feng, 2012: Analyses of hydrometeor identification based on X-band polarimetric radar. *Climatic and Environmental Research*, **17**, 925–936. (in Chinese)

Loney, M. L., D. S. Zrnic, J. M. Straka, and A. V. Ryzhkov, 2002: Enhanced polarimetric radar signatures above the melting level in a supercell storm. *J. Appl. Meteor.*, **41**, 1179–1194, https://doi.org/10.1175/1520-0450(2002)041<1179:EPRSAT>2.0.CO;2.

Luo, Y. L., and Coauthors, 2016: The southern China monsoon rainfall experiment (SCMREX). *Bull. Amer. Meteor. Soc.*, **98**, 999–1013, https://doi.org/10.1175/BAMS-D-15-00235.1.

Mohr, C. G., L. J. Miller, R. L. Vaughan, and H. W. Frank, 1986: The merger of mesoscale datasets into a common Cartesian format for efficient and systematic analyses. *J. Atmos. Oceanic Technol.*, **3**, 143–161, https://doi.org/10.1175/1520-0426(1986)003<0143:TMOMDI>2.0.CO;2.

Pan, Y. J., K. Zhao, and Y. N. Pan, 2010: Single-doppler radar observations of a high precipitation supercell accompanying the 12 April 2003 Severe Squall Line in Fujian Province. *Acta Meteorologica Sinica*, **24**, 50–65.

Park, H. S., A. V. Ryzhkov, D. S. Zrnić, and K. E. Kim, 2009: The hydrometeor classification algorithm for the polarimetric WSR-88D: Description and application to an MCS. *Wea. Forecasting*, **24**, 730–748, https://doi.org/10.1175/2008WAF2222205.1.

Ryzhkov, A. V., S. E. Giangrande, V. M. Melnikov, and T. J. Schuur, 2005: Calibration issues of dual-polarization radar measurements. *J. Atmos. Oceanic Technol.*, **22**, 1138–1155, https://doi.org/10.1175/JTECH1772.1.

Richardson, L. M., W. David Zittel, R. R. Lee, V. M. Melnikov, I. L. Ice, and J. G. Cunningham, 2017: Bragg scatter detection by the WSR-88D. Part I: Algorithm development. *J. Atmos. Oceanic Technol.*, **34**, 479–493, https://doi.org/10.1175/JTECH-D-16-0030.1.

Ryzhkov, A. V., 2007: The impact of beam broadening on the quality of radar polarimetric data. *J. Atmos. Oceanic Technol.*, **24**, 729–744, https://doi.org/10.1175/JTECH2003.1.

Schuur, T. J., A. V. Ryzhkov, and P. L. Heinselman, D. Zrnic, and D. Burgess, 2003: Observations and classification of echoes with the polarimetric WSR-88D radar. NOAA/National Severe Storms Laboratory Rep, 46 pp.

Schuur, T. J., H. S. Park, A. V. Ryzhkov, and H. D. Reeves, 2012: Classification of precipitation types during transitional winter weather using the RUC model and polarimetric radar retrievals. *J. Appl. Meteor. Climatol.*, **51**, 763–779, https://doi.org/10.1175/JAMC-D-11-091.1.

Straka, J. M., and D. S. Zrnić, 1993: An algorithm to deduce

hydrometeor types and contents from multi-parameter radar data. *Preprints, 26th Conf. on Radar Meteorology*. Norman, OK, Amer. Meteor. Soc., 513–515.

Straka, J. M., 1996: Hydrometeor fields in a supercell storm as deduced from dual-polarization radar. *Preprints, 18th Conf. on Severe Local Storms*. San Francisco, CA, Amer. Meteor. Soc., 551–554.

Su, D. B., J. L. Ma, Q. Zhang, and D. R. Lu, 2011: Preliminary research on method of hail detection with X band dual linear polarization radar. *Meteorological Monthly*,, **37**, 1228–1232. (in Chinese)

Vivekanandan, J., D. S. Zrnić, S. Ellis, D. Oye, A. V. Ryzhkov, and J. M. Straka, 1999: Cloud microphysics retrieval using S-band dual-polarization radar measurements. *Bull. Amer. Meteor. Soc.*, **80**, 381–388, https://doi.org/10.1175/1520-0477(1999)080<0381:CMRUSB>2.0.CO;2.

Wakimoto, R. M., and V. N. Bringi, 1988: Dual-polarization observations of microbursts associated with intense convection: The 20 July storm during the MIST project. *Mon. Wea. Rev.*, **116**, 1521–1539, https://doi.org/10.1175/1520-0493(1988)116<1521:DPOOMA>2.0.CO;2.

Wang, H., Y. L. Luo, and B. J. Jou, 2014: Initiation, maintenance, and properties of convection in an extreme rainfall event during SCMREX: Observational analysis. *J. Geophys. Res.*, **119**, 13 206–13 232, https://doi.org/10.1002/2014JD022339.

Wei, Q., Z. Q. Hu, L. P. Liu, and L. L. Wu, 2016: C-band polarization radar data preprocessing and its application to rainfall estimation. *Plateau Meteorology*, **35**, 231–243, https://doi.org/10.7522/j.issn.1000-0534.2014.00131. (in Chinese)

Xiao, Y. J., B. Wang, X. H. Chen, J. W. Cao, and X. M. Yang, 2012: Differential phase data quality control of mobile X-band dual-polarimetric Doppler weather radar. *Plateau Meteorology*, **31**, 223–230. (in Chinese)

Yu, X. D., Y. Y. Zheng, Y. F. Liao, Y. Q. Yao, and C. Fang, 2008: Observational investigation of a tornadic heavy precipitation supercell storm. *Chinese Journal of Atmospheric Sciences*, **32**, 508–522. (in Chinese)

Zhang, J., and Coauthors, 2011: National Mosaic and Multi-Sensor QPE (NMQ) system-Description, results and future plans. *Bull. Amer. Meteor. Soc.*, **92**, 1321–1338, https://doi.org/10.1175/2011BAMS-D-11-00047.1.

Zhang, J., Y. Qi, D. Kingsmill, and K. Howard, 2012: Radar-based quantitative precipitation estimation for the cool season in complex terrain: Case studies from the NOAA Hydrometeorology Testbed. *J. Hydrometeor.*, **13**, 1836–1854, https://doi.org/10.1175/JHM-D-11-0145.1.

Zrnić, D. S., and A. V. Ryzhkov, 1999: Polarimetry for weather surveillance radars. *Bull. Amer. Meteor. Soc.*, **80**, 389–406, https://doi.org/10.1175/1520-0477(1999)080<0389:PFWSR>2.0.CO;2.